Structural basis of the mechanism and inhibition of a human ceramide synthase

Tomas C. Pascoa[1†], Ashley C.W. Pike[1], Christofer S. Tautermann[2], Gamma Chi[1], Michael Traub[2], Andrew Quigley[1,4], Rod Chalk[1], Saša Štefanic[3,5], Sven Thamm[2], Alexander Pautsch[2], Elisabeth P. Carpenter[1†], Gisela Schnapp[2†], David B. Sauer[1†]

[1] Centre for Medicines Discovery, Nuffield Department of Medicine, University of Oxford, Oxford, UK

[2] Boehringer Ingelheim Pharma GmbH & Co KG, Birkendorfer Straße 65, 88397, Biberach, Germany

[3] Institute of Parasitology, Vetsuisse and Medical Faculty, University of Zürich, Zürich, Switzerland

[4] Present address: Membrane Protein Laboratory, Research Complex at Harwell, Diamond Light Source Ltd, Harwell Science and Innovation Campus, Didcot, UK

[5] Present address: Nanobody Service Facility, University of Zurich, AgroVet-Strickhof, 8315, Lindau, Switzerland

[†] Correspondence to: T.C.P. (tomas.pascoa@cmd.ox.ac.uk), E.P.C. (lizcarpen1@gmail.com), G.S. (gisela.schnapp@boehringer-ingelheim.com) or D.B.S. (david.sauer@cmd.ox.ac.uk)

Abstract

Ceramides are bioactive sphingolipids that play pivotal roles in regulating cellular metabolism. Ceramides and dihydroceramides are synthesized by a family of six ceramide synthase enzymes (CerS), each with distinct specificity for the acyl-CoA substrate. Importantly, the acyl chain length plays a key role in determining the physiological function of ceramides, as well as their role in metabolic disease. Ceramide with an acyl chain length of 16 carbons (C16 ceramide) has been implicated in obesity, insulin resistance and liver disease, and the C16 ceramide-synthesizing CerS6 is regarded as an attractive drug target for obesity-associated disease. Despite their importance, the molecular mechanism underlying ceramide synthesis by CerS enzymes remains poorly understood. Here, we report cryo-

electron microscopy structures of human CerS6, capturing covalent intermediate and product-bound states. These structures, together with biochemical characterization using intact protein and small molecule mass spectrometry, reveal that CerS catalysis proceeds via a ping-pong reaction mechanism involving a covalent acyl-enzyme intermediate. Notably, the product-bound structure was obtained upon reaction with the mycotoxin fumonisin B_1, providing new insights into its inhibition of CerS. These results provide a framework for understanding the mechanisms of CerS function, selectivity, and inhibition, and open new directions for future drug discovery targeting the ceramide and sphingolipid pathways.

Introduction

Ceramides are the precursors for the synthesis of complex sphingolipids and are bioactive lipids with crucial roles in signaling. In particular, ceramides have been proposed to act as key metabolic sensors to promote fatty acid utilization and storage during excessive fatty acid availability[1]. However, abnormal ceramide accumulation is associated with metabolic dysfunction, and elevated levels of ceramides have been observed in obesity-related metabolic disorders such as diabetes, non-alcoholic fatty liver disease (NAFLD) and non-alcoholic steatohepatitis (NASH)[2-4].

Ceramides are composed of a sphingosine (d18:1) long-chain base with an N-linked acyl chain, the length of which is critical to the lipids' biological functions and roles in pathophysiology[5]. For example, C16:0 ceramide is the most common ceramide in adipose tissue and its levels are elevated in this tissue of obese humans[2]. In addition, insulin resistance is correlated with plasma C16:0 and C18:0 ceramides, subcutaneous adipose tissue C16:0 ceramides, and hepatic C16:0 and C18:0 ceramides[6-8]. Moreover, the levels of total

51 ceramides and C16:0, C22:0 and C24:1 dihydroceramides were found to be elevated in the
52 liver of insulin-resistant patients with NASH[3].

53 In mammals, *de novo* synthesis of ceramides is preceded by synthesis of dihydroceramides
54 through the N-acylation of the sphingoid long-chain base sphinganine (dihydrosphingosine;
55 d18:0) by one of six ceramide synthases (CerS1-6)[9]. The resulting dihydroceramides are
56 subsequently converted into ceramides by one of two dihydroceramide Δ4-desaturases
57 (DES1-2)[10]. Alternatively, CerS can directly re-acylate recycled sphingosine, in the salvage
58 pathway[11]. Of these enzymes, recent observations from human and mouse studies have
59 highlighted CerS6 as an attractive target for treating obesity-associated metabolic disease,
60 including type 2 diabetes and NASH[2,5,12-14]. Deletion of *CerS6* in mice granted protection
61 against diet-induced obesity, steatohepatitis, and insulin resistance[2,14], and liver-specific
62 deletion improved glucose tolerance and mitochondrial morphology[14]. Strikingly, this effect
63 was shown to only occur in CerS6$^{\Delta/\Delta}$ mice but not in CerS5$^{\Delta/\Delta}$ mice, though both show a
64 preference for C16-CoA and therefore primarily produce C16 ceramides[15] and hepatic C16:0
65 ceramide levels were reduced in both knock-outs[14]. This surprising effect was found to be a
66 result of the specific interaction of CerS6-derived C16:0 sphingolipids in mitochondria with
67 the mitochondrial fission factor (Mff)[14]. This revealed that the subcellular localization of
68 ceramide production can lead to drastically different physiological outcomes[14]. In further
69 support of the therapeutic potential of inhibiting CerS6, ablation of the protein's expression in
70 an obese insulin resistance mouse model led to reduced body fat and improved oral glucose
71 tolerance and insulin sensitivity[12].

72 Central to its enzymatic function, CerS contain a TRAM-Lag1-CLN8 (TLC) homology
73 domain[16], which includes a 52-residue Lag1p motif containing conserved histidines and
74 aspartates required for activity[17,18]. In addition, CerS2-6 contain a non-essential Hox-like

75 domain between TM1-2[19], flanked by two essential and conserved positively charged
76 residues[20]. The activity of each CerS is subject to complex regulation, which includes
77 phosphorylation[21], glycosylation[22], dimerisation[23] and other protein-protein interactions[24,25].
78 The six mammalian CerS also have different acyl chain-length specificities and tissue
79 expression patterns, further influencing the tissue-specific distribution of the different
80 ceramides[5,9,26]. However, the molecular mechanisms underlying synthesis and regulation of
81 ceramides and dihydroceramides remain unclear.

82 Despite the interest in pharmacologically reducing CerS6 activity, at present, no specific
83 inhibitors have been described for this family member. The best characterized CerS inhibitor
84 is fumonisin B_1 (FB_1), the most prevalent member of the fumonisin family of mycotoxins
85 produced by *Fusarium* species. FB_1 is a potential carcinogen and teratogen and therefore of
86 significant concern as it is a common contaminant in maize, rice, other cereals, and cereal-
87 based food stocks[27-29]. FB_1 is a potent non-selective inhibitor of all human CerS, and is
88 competitive towards both sphinganine and acyl-CoA substrates[30]. In addition, FTY720
89 (fingolimod, Gilenya), a prodrug administered to functionally antagonize the sphingosine-1-
90 phosphate receptor 1 in the treatment of multiple sclerosis, is also a non-selective CerS
91 inhibitor[31,32]. Further, a non-phosphorylatable analogue of FTY720, P053, has recently been
92 shown to potently and selectively inhibit CerS1[33], showcasing the possibility of achieving
93 isoform-specific CerS inhibition.

94 Here, to understand the molecular basis of ceramide and dihydroceramide synthesis by the
95 ceramide synthases, we employed a combination of cryogenic electron microscopy (cryo-
96 EM), intact protein mass spectrometry, and small-molecule high-resolution and tandem mass
97 spectrometry to probe the catalytic mechanism of human CerS6.

98

99 # Results

100 ## Cryo-EM structure of human CerS6

101 We recombinantly expressed the human CerS6 protein, truncated at Asp350 to remove the
102 predicted disordered C-terminus, in suspension-adapted HEK293 cells using the BacMam
103 system. The protein was purified in glyco-diosgenin (GDN), yielding a mixture of
104 monomeric and dimeric species on size-exclusion chromatography (Extended Data Fig. 1a-
105 d). While we selected the dimer species for structural studies to maximize particle size and
106 possible symmetry for single-particle cryo-EM, its relatively low molecular weight (84 kDa)
107 is still challenging for current methods. We therefore raised camelid nanobodies against the
108 purified protein and solved the structure of a CerS6 dimer with one nanobody bound per
109 monomer at a nominal resolution of 3.2 Å resolution (Fig. 1a,b; Extended Data Table 1;
110 Extended Data Fig. 2). The CerS6-Nb22 complex was well resolved throughout the
111 membrane-spanning region, but the Hox-like domain was less well-defined. This allowed for
112 unambiguous tracing of CerS6 and Nb22 with the exception of the Hox-like domains, where
113 residues 72-119 were fitted into the envelope of the cryo-EM map as rigid bodies (see
114 Methods) (Extended Data Fig. 2e; Extended Data Fig. 3a).

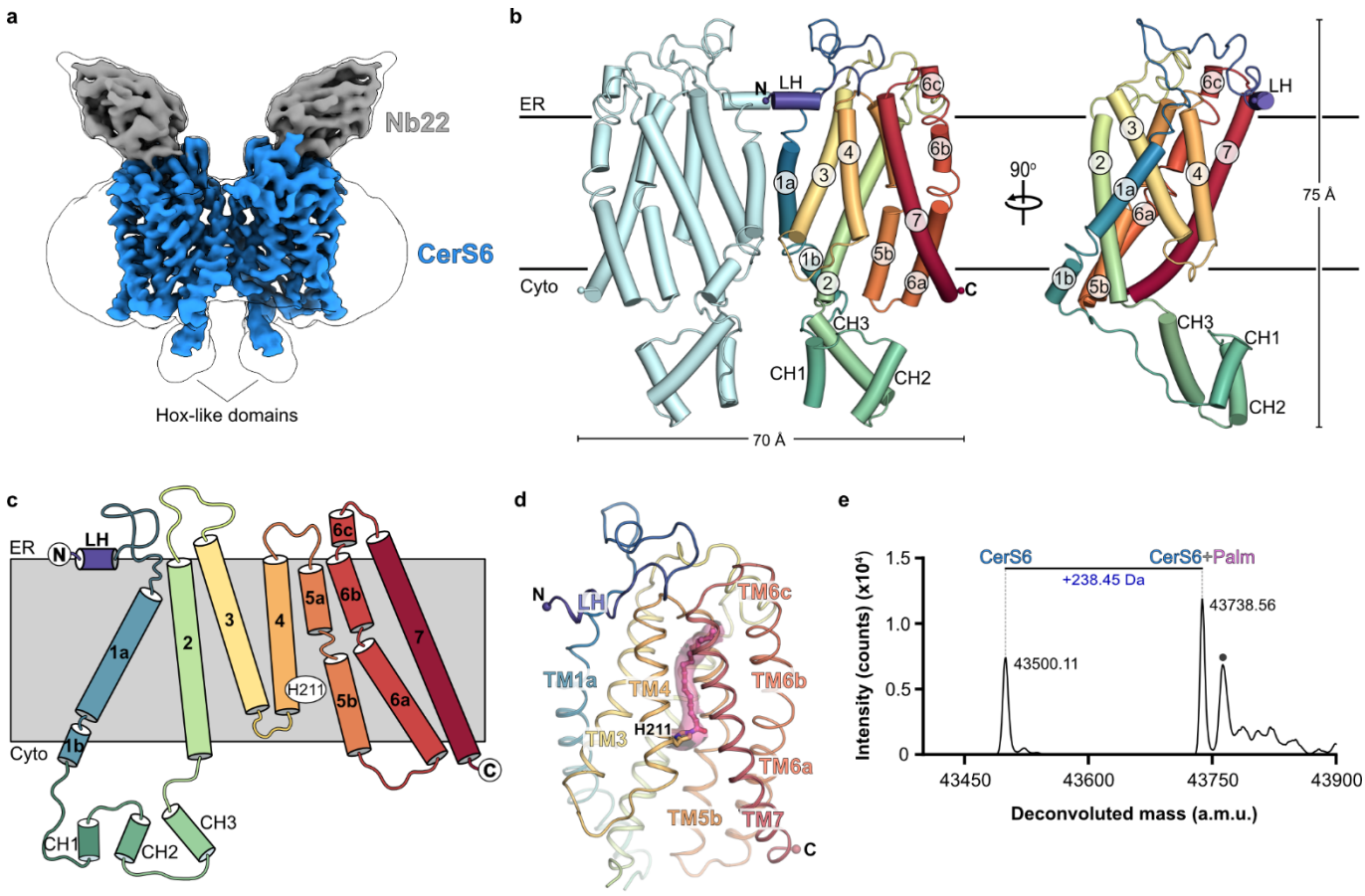

Figure 1. Cryo-EM structure of human CerS6. a, Cryo-EM map of the CerS6 dimer (blue) with one copy of Nb22 (gray) bound to each CerS6 monomer. **b,** Overall cartoon cylinder representation of the CerS6 dimer structure. One of the monomers is rainbow-coloured from purple (N-terminus) to red (C-terminus). **c,** schematic representation of the CerS6 7-TM helix topology. **d,** Cartoon representation of the transmembrane domain of a CerS6 monomer. The covalent acyl-imidazole species is shown in stick representation (acyl chain: pink carbon atoms), and the Coulombic potential map for this covalent species is shown as a pink transparent surface. The Hox-like domain was omitted for clarity. **e,** Denaturing intact protein MS analysis of purified CerS6 protein, revealing the presence of a covalent modification (+238.45 Da) which matches the expected mass shift corresponding to covalent attachment of a palmitoyl (Palm; C16:0) chain. This adduct peak was present in all purifications tested (n=6).

The cryo-EM structure reveals a CerS6 homodimer with one nanobody bound per monomer on the luminal face. Each monomer has 7 transmembrane helices (Fig. 1b,c), with the dimer interface formed by TM1a, the C-terminal end of TM3, and the TM3-TM4 loop. The TLC

131 domain (TM2-7) forms a barrel containing two 3-TM units arranged as inverted repeats
132 (Extended Data Fig. 4a), while TM1 is attached to the outside of the barrel through contacts
133 with TM2/3. The TM2-7 barrel is assembled around a central cavity, which is open to the
134 cytoplasm and closed to the ER lumen by a loop between TM6-7. This central cavity has a
135 large cytoplasmic opening (approximately 23 x 12 Å), creating a vestibule that funnels
136 towards the midpoint of the membrane, where it forms a ~5 Å wide tunnel that stretches
137 towards the ER side.

138 Interestingly, the fold of the TM2-7 barrel of CerS6 resembles that of the 6-TM barrels found
139 in very-long-chain fatty acid elongase ELOVL7[34] and TMEM120A/B[35,36], as identified by
140 DALI[37]. Additionally, a structurally homologous 6-TM barrel is predicted in the AlphaFold2
141 models of 3-hydroxyacyl-CoA dehydratases (HACD1-4) (Extended Data Fig. 4b), which
142 participate in the same four-enzyme acyl-CoA elongation cycle as ELOVLs[38]. The
143 observation that different acyl-CoA-modifying enzyme families share a similar 6-TM barrel
144 structure is intriguing, suggesting that this architecture is likely optimized for the specific
145 recognition and reaction with acyl-CoA substrates.

146

147 **CerS6 co-purifies with a covalently bound C16:0 acyl chain**

148 Surprisingly, the cryo-EM density map revealed the presence of a long density extending
149 from near the membrane mid-point to the occluded ER end of the central cavity, spanning the
150 entire length of the narrow tunnel (Fig. 1d; Fig. 2a). This density was continuous between
151 protein and the unknown molecule, suggesting a covalent modification by a lipid. To probe
152 the presence of covalent adducts, we performed denaturing intact protein mass spectrometry
153 (MS) analysis of purified protein samples, and identified a +238.45 Da mass shift (Fig. 1e
154 and Extended Data Fig. 1f,g). Notably, this adduct mass agrees with a covalently attached

155 C16:0 acyl chain (theoretical: +238.41 Da). Strikingly, the shape and length of the density in
156 the cryo-EM map is also consistent with a bound C16 acyl chain. A covalent bond is seen
157 linking the acyl chain to the imidazole Nε of His211 (TM4) (Fig. 2b; Extended Data Fig. 3b),
158 an absolutely conserved histidine that is required for CerS activity[17,18]. Thus, based on the
159 extended density in the cryo-EM map and the observed mass adduct, we have modelled a
160 palmitoyl (C16:0) chain covalently attached to His211.

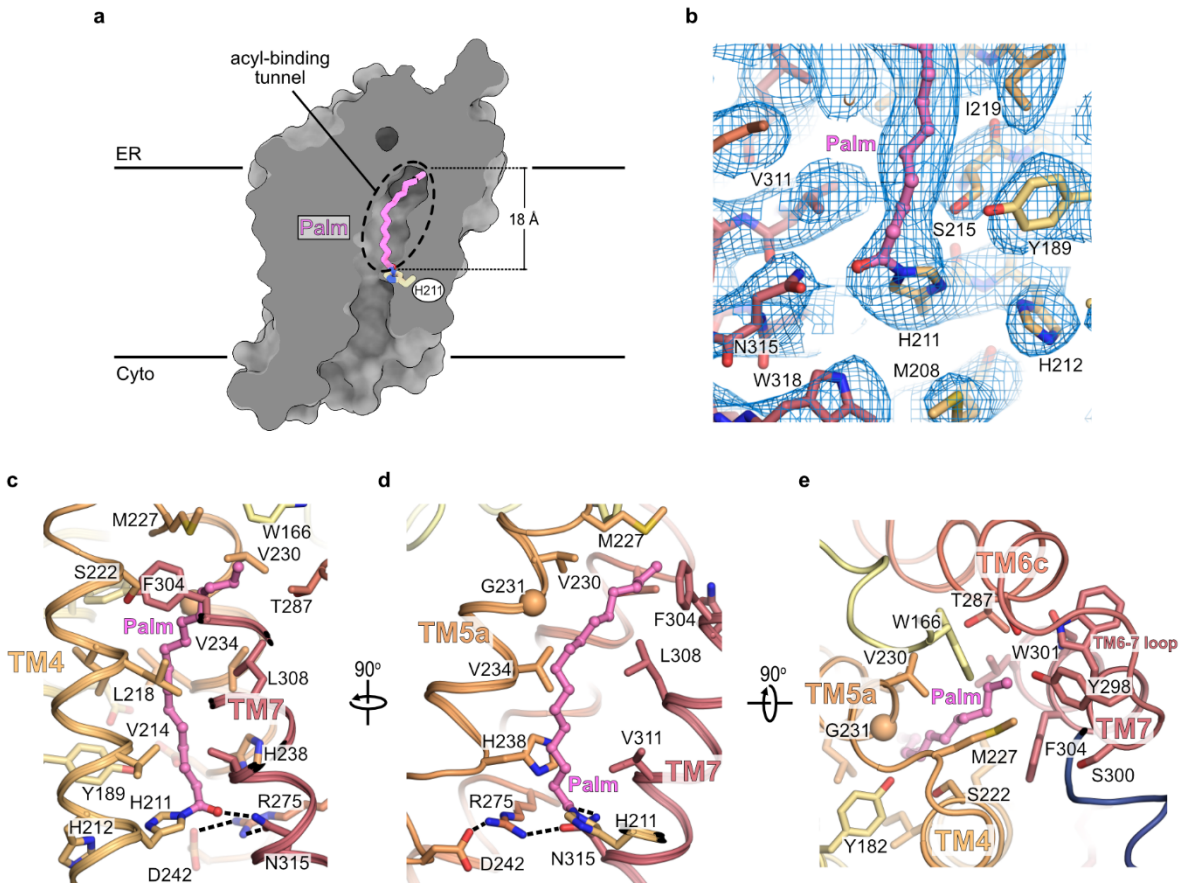

161

162 **Figure 2. CerS6 contains an acyl chain-binding tunnel buried deep in the membrane. a**, Cutaway
163 molecular surface representation of the CerS6 transmembrane region, revealing the presence of a long
164 central cavity spanning the entire length of the protein. The palmitoyl chain covalently attached to
165 His211 is bound in a narrow tunnel on the ER luminal half of the central cavity. **b**, Coulombic
166 potential map in the region around the covalent linkage of the acyl chain to His211. **c-e**, CerS6's acyl-
167 binding tunnel, viewed from the **(c,d)** membrane plane or **(e)** from the ER face. Side-chains lining and
168 capping the tunnel are shown as sticks. Hydrogen bonds in the active site are shown as dashed lines.

169

170 The acyl chain is surrounded in the narrow tunnel primarily by hydrophobic side chains from
171 TM4, TM5 and TM7 (Fig. 2c-e). The tunnel is sealed at the ER end by the TM6-7 loop (Fig.
172 2e), revealing how the chain-length preference of CerS6 for C16-CoA is determined by
173 limiting the number of carbons that can fit in the acyl-binding tunnel. This observation is in
174 agreement with earlier reports that this loop determines CerS acyl chain specificity[22].

175

176 **Catalysis by CerS6 proceeds via a ping-pong mechanism**

177 Acyltransferases catalyze two-substrate, two-product reactions that can proceed via either
178 ternary-complex or double-displacement (ping-pong) mechanisms[39]. In a ternary-complex
179 mechanism, both the acyl donor and acceptor bind simultaneously and the enzyme catalyzes
180 the direct acyl transfer from one substrate to the other. In contrast, a ping-pong mechanism
181 involves two independent steps. Initially, reaction with the first substrate (the acyl donor)
182 results in the transfer of the acyl chain to a nucleophilic residue, forming a covalent acyl-
183 enzyme intermediate. This acyl chain is then transferred to the second substrate (the acyl
184 acceptor) in the second step of the reaction.

185 The CerS6 structure reveals that there is not enough space for both substrates to bind in the
186 central cavity and access the active site at the same time, thereby indicating a ternary-
187 complex mechanism is unlikely. Furthermore, the C16:0 chain covalently attached to the
188 conserved His211 fits with CerS6's selectivity for palmitoyl-CoA and suggests that this
189 species could correspond to the acyl-enzyme intermediate of a ping-pong type reaction
190 mechanism. To investigate whether the acylated enzyme species corresponds to a real
191 catalytic intermediate, we incubated the purified protein with the enzyme's second substrate,
192 the long-chain base sphinganine (Fig. 3a). Using denaturing intact protein MS, we observed
193 the complete loss of the C16:0-modified protein after sphinganine addition (Fig. 3b and

194 Extended Data Fig. 5a). Furthermore, high-resolution mass spectrometry (HRMS) revealed
195 that incubation of the acylated protein with sphinganine led to the production of C16:0
196 dihydroceramide (observed *m/z*: 540.5380; theoretical *m/z*: 540.5350; mass error: +5.55 ppm)
197 (Fig. 3c). Overall, these results clearly demonstrate that sphinganine reacts with the acyl-
198 enzyme intermediate to de-acylate the enzyme and generate the expected reaction product of
199 dihydroceramide, thus supporting a ping-pong reaction mechanism for CerS6. Taken together
200 with the structural data, this implies that His211 acts as the nucleophile in the first step of the
201 reaction.

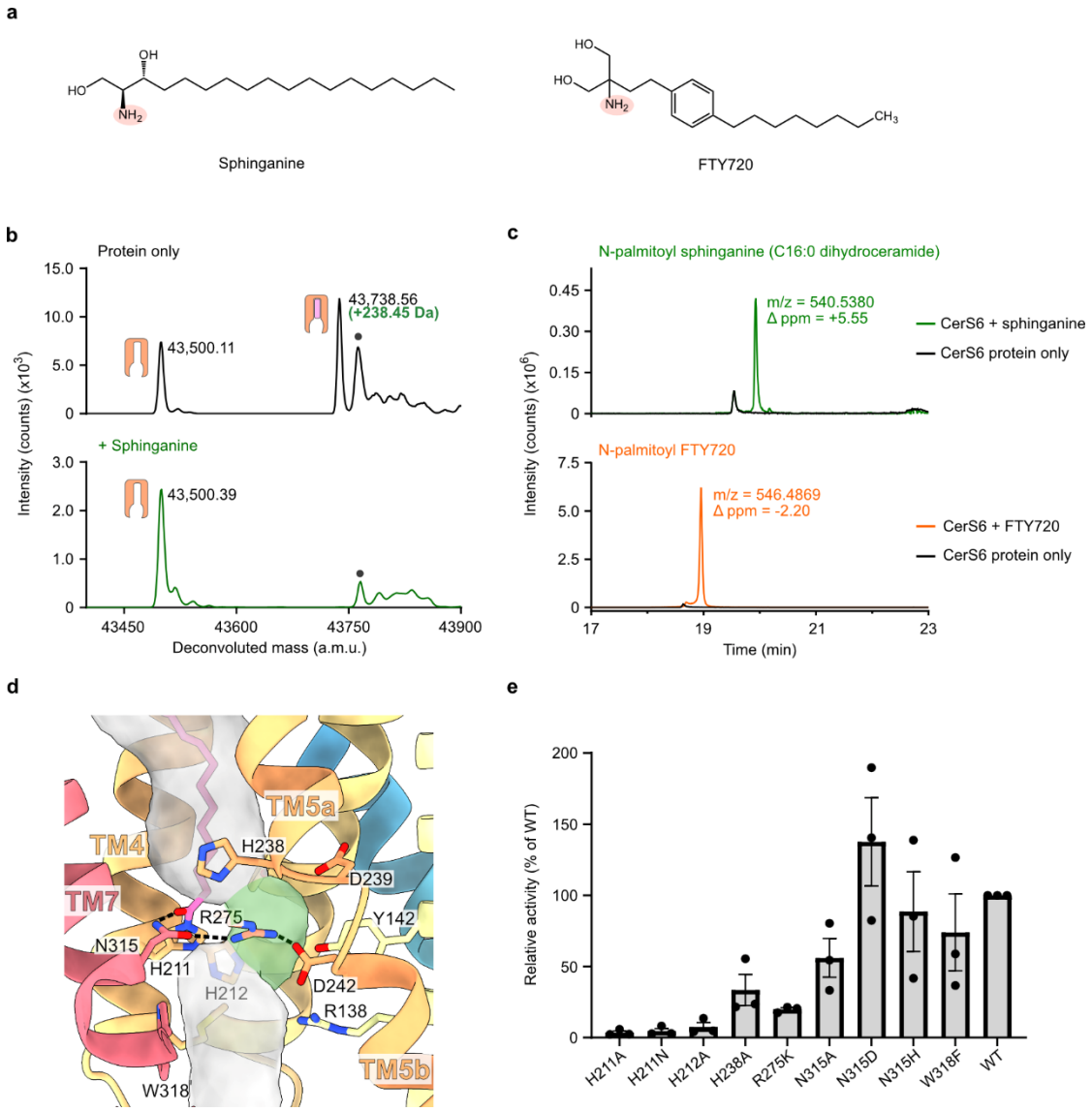

202

203 **Figure 3. Unraveling the catalytic mechanism of CerS6 using mass spectrometry. a,** chemical
204 structures of the natural long-chain base substrate sphinganine (dihydrosphingosine) and the drug
205 FTY720 (fingolimod, Gilenya). The homologous primary amines are highlighted in salmon. **b**, Intact
206 mass analysis of protein samples after incubation in the absence of substrates (black) or in the
207 presence of sphinganine (green) (n = 3 biological replicates; see Extended Data Fig. 5 for replicate
208 traces). Deconvoluted mass peaks are indicated as follows: unmodified enzyme, orange icon; covalent
209 acyl-enzyme species, orange and pink icon; background species present in all traces, gray circle. **c**,
210 LC-HRMS detection of the reaction products. Extracted ion chromatograms (EICs) for the expected
211 $[M+H]^+$ ions of each of the reaction products after incubation of the acyl-enzyme intermediate with
212 sphinganine (C16:0 dihydroceramide, green) or FTY720 (N-palmitoyl FTY720, orange). EICs
213 obtained after incubation in the absence of substrates are shown in black. **d**, CerS6's active site,
214 viewed from the plane of the membrane. The central cavity is shown as a transparent gray surface,
215 highlighting the presence of a side pocket (highlighted in green) adjacent to the acyl carbonyl.
216 Hydrogen bonds are shown as dashed lines. **e**, Mutational analysis of the CerS6 active site by
217 comparison of the C16:0 dihydroceramide synthase activity of wild-type (WT) and active site
218 mutants. n=3 independent biological replicates. Gray bars correspond to the mean of the biological
219 replicates. Data points represent each biological replicate, corresponding to the mean of four technical
220 replicates. Error bars show the SEM.

221

222 Notably, the CerS substrate sphinganine and FTY720 are chemically similar (Fig. 3a), with
223 potential clinical consequences to drug pharmacokinetics as 15% of FTY720 becomes N-
224 acylated in human subjects[40]. Although the major N-acyl FTY720 metabolites identified were
225 N-stearoyl and N-2-hydroxystearoyl FTY720, there is evidence suggesting that a small
226 amount of N-palmitoyl (C16:0) FTY720 is formed[40]. Which enzyme catalyzes the N-
227 acylation of FTY720 has not been determined, but a putative role for CerS enzymes or the
228 reverse reaction of ceramidases has been proposed[40]. Incubation of acyl-CerS6 with FTY720
229 results in a small increase in the protein's thermostability, suggesting it binds to the purified
230 enzyme (Extended Data Fig. 1e). To investigate whether purified CerS6 can N-acylate
231 FTY720 *in vitro*, we incubated the enzyme with this compound, and subsequently identified
232 C16:0 FTY720 in the reaction mixture (observed *m/z*: 546.4869; theoretical *m/z*: 546.4881;

233 mass error: -2.20 ppm) (Fig. 3c), the expected product of a reaction between FTY720 and the
234 CerS6 bound acyl chain. The proposed structure of this C16:0 FTY720 reaction product was
235 further validated based on the product ion MS/MS spectrum of its $[M+H]^+$ ion (Extended
236 Data Fig. 6). However, no obvious loss of the acyl-enzyme mass peak was observed when the
237 reaction mixture was analyzed by denaturing intact protein MS (Extended Data Fig. 5b),
238 suggesting that FTY720 is a poor acyl acceptor for acylated CerS6.

239

240 **Highly conserved residues line the catalytic site**

241 CerS6's Lag1p motif (Arg202-Tyr253) (TM4-5) contains the highly conserved
242 His211/His212 (TM4) and Asp239/Asp242 (L5a-b/TM5), which have been previously
243 suggested to be located in the catalytic site and have been shown to be essential for function
244 in mammalian CerS[17] and *S. cerevisiae* Lag1p[18].

245 Examining the CerS6 structure, we noted these residues line the central cavity near the mid-
246 point of the membrane (Fig. 3d). Notably, the co-purified covalently linked C16:0 chain is
247 covalently attached to the first histidine of the Lag1p motif (His211) (Fig. 2a-d), which
248 appears to act as the nucleophile in the first step of the reaction and is required for CerS6
249 function (Fig. 3e). Although the observation that the mechanism of CerS6 involves a
250 nucleophilic histidine was surprising - as cysteines or serines are more commonly employed
251 as nucleophiles - there are multiple well-documented examples of other enzymes using
252 nucleophilic histidines in their catalytic mechanisms[34,41-45].

253 Histidine nucleophiles are typically oriented and activated by hydrogen-bonding between a
254 proton at Nδ of the imidazole ring and a hydrogen bond acceptor, ensuring that Nε remains
255 unprotonated[34,42,46]. Examining our structure, we noted the proximity of His212 to the

256 acylated His211 in CerS6, which immediately suggested this residue is the necessary
257 hydrogen bond acceptor. While the Nδ of His212 is located 3.84 Å away from the Nδ of
258 His211, it is plausible that the two side chains may interact in the acyl-CoA-bound state.
259 Indeed, we found that mutation of His212 to alanine results in the complete loss of activity
260 (Fig. 3e). Residues equivalent to His212 of CerS6 are also essential in the homologous mouse
261 and human CerS1[17,47] and yeast Lag1p[18]. This demonstrates the second histidine plays a key
262 role in catalysis, and explains the pathogenic effect of mutating the equivalent His of CerS1
263 to a Gln in patients with progressive myoclonic epilepsy and dementia[47]. Moreover, we have
264 recently demonstrated that the reaction of human ELOVL7 with acyl-CoA substrates also
265 involves a double histidine motif, where the first histidine acts as a nucleophile and is
266 activated by hydrogen-bonding to the second[34]. Strikingly, structural alignment of CerS6 and
267 ELOVL7 places the histidine pairs in equivalent positions (Extended Data Fig. 4c),
268 suggesting that these residues may play similar roles in the first step of their respective
269 reactions.

270 Formation of the acyl-enzyme intermediate proceeds via an oxyanion transition state, which
271 is usually stabilized by hydrogen bonding. Within the acyl-CerS6 structure, the carbonyl
272 oxygen of the covalently attached C16:0 chain is within hydrogen-bonding distance (2.8 Å)
273 of the Nδ of Asn315 (TM7). Based on the proximity of these moieties, we hypothesized that
274 this interaction could stabilize the formation of the oxyanion transition state during catalysis.
275 Consistent with this notion, an Asn is present at the equivalent position in CerS1, and CerS2-
276 5, Lag1p and Lac1p have a His at this position (Extended Data Fig. 7) which may likewise
277 act as a hydrogen-bond donor. Indeed, we found that an Asn315His mutant preserves activity.
278 Surprisingly, however, mutation of Asn315 to either an Ala or an Asp did not result in loss of
279 activity (Fig. 3e). It is unclear if the hydrogen bond in the wild-type structure is not required
280 for function, or if these mutations allow a water molecule to enter the reaction site and act as

281 a substitute hydrogen bond acceptor. Asn315 is involved in a hydrogen-bonding network
282 involving the conserved Arg275 (L6a-b) and Asp242 (TM5b). We found that an Arg275Lys
283 mutant retained only approximately 20 % of wild-type activity (Fig. 3e), suggesting that the
284 interactions established by the guanidino group of Arg275 to align neighbouring residues in
285 the active site are important for function.

286 There is a third histidine on TM5a which is conserved in mammalian CerS but is a
287 methionine in yeast Lag1p and Lac1p, and is therefore of ambiguous importance to the
288 enzymes' reaction cycle. In the CerS6 structure this residue, His238, is located above the
289 acyl-imidazole carbonyl and lays against the hydrocarbon chain (Fig. 3d). We found that
290 mutation of this His238 to alanine reduced activity by over 50 % (Fig. 3e), and therefore
291 suggest this residue may participate in aligning the acyl chain.

292 Finally, we noticed the presence of a side pocket in the active site of CerS6, adjacent to
293 His211 (Fig. 3d) and lined by Tyr142 (TM2), Tyr189 (TM3), His212 (TM4), Asp239 (L5a-
294 b), Asp242 (TM5b) and Arg275 (L6a-b). The position and chemistry of this pocket relative to
295 the carbonyl of the acyl-enzyme intermediate suggests this is likely to be the site where the
296 amino alcohol moiety of the second (long-chain base) substrate binds. Supporting this notion,
297 the residues of this pocket are highly conserved (Extended Data Fig. 7). This pocket therefore
298 likely ensures the primary amine of the long-chain base is ideally located for a nucleophilic
299 attack on the carbonyl carbon of the acyl-imidazole intermediate in the second step of the
300 reaction.

301

302 **Structure of N-acyl fumonisin B_1-bound CerS6**

303 Having captured the intermediate state of the CerS6 enzyme, we next set out to examine the
304 structural basis of CerS inhibition by FB_1. To this end, we incubated purified acyl-CerS6 with
305 fumonisin B_1, and determined the complex's structure to a nominal resolution of 2.95 Å (Fig.
306 4a,b and Extended Data Fig. 8). In comparison with the covalent intermediate state, the
307 overall structure of each CerS6 monomer did not change (transmembrane region backbone
308 RMSD = 0.39 Å), although the flexible Hox-like domains rotated by approximately 10°.

309 The cryo-EM map of the putative FB_1-bound complex contains a long, continuous non-
310 protein density starting within the ER luminal end of the narrow tunnel and extending to the
311 cytoplasmic entrance to the central cavity (Fig. 4a and Extended Data Fig. 3c,d). The
312 observed density is too long to be FB_1 alone. Notably, incubation of palmitoyl-CerS6 with
313 FB_1 completely removed the acyl group from the enzyme (Fig. 4c and Extended Data Fig. 5a
314 and generated C16:0-fumonisin B_1 (observed *m/z*: 960.6260; theoretical *m/z*: 960.6254; mass
315 error: +0.62 ppm) (Fig. 4d). Noting the covalent bond between the enzyme and the palmitoyl
316 group has been replaced by a bond to the toxin, we modeled this density as C16:0-FB_1 (Fig.
317 5a and Extended Data Fig. 3c). These results indicate FB_1 has reacted with the covalent acyl-
318 enzyme intermediate, releasing His211 and generating the N-acyl FB_1 product. This product
319 remains bound to the enzyme, thus acting as an inhibitor. This finding is consistent with
320 earlier reports that CerS enzymes can N-acylate FB_1 in cultured cells and in rats[48,49].

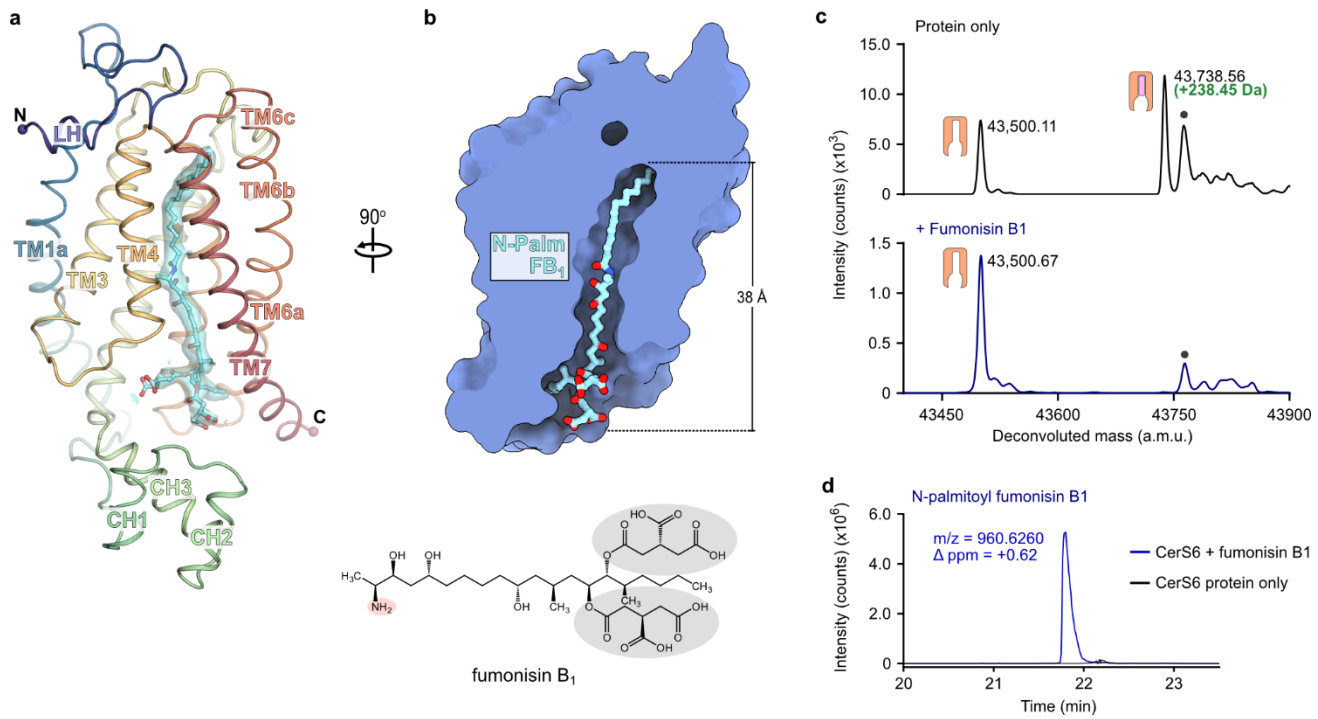

321

322 **Figure 4. Cryo-EM structure of CerS6 in complex with N-palmitoyl fumonisin B_1. a**, Cartoon
323 representation of CerS6 with bound N-palmitoyl fumonisin B_1 (shown as sticks; cyan carbon atoms).
324 The cryo-EM density of the bound product is shown as a transparent cyan surface. **b**, Cutaway
325 molecular surface representation, revealing that the N-palmitoyl fumonisin B_1 species occupies the
326 entire length of the central cavity. The Hox-like domain has been omitted for clarity. **c**, Intact mass
327 analysis of protein samples after incubation in the absence of substrates (black) or in the presence of
328 the mycotoxin fumonisin B_1 (blue) (n = 3 biological replicates; see Extended Data Fig. 5 for replicate
329 traces). **d,** LC-HRMS detection of N-palmitoyl fumonisin B_1. The EIC for its expected $[M+H]^+$ ion is
330 shown after incubation of the acyl-enzyme intermediate with fumonisin B_1 (blue) or in the absence of
331 the toxin (black). *Inset:* chemical structure of fumonisin B_1. Its primary amine (salmon circle) and
332 tricarballylic acid groups (gray circles) are highlighted.

333

334 The N-acyl FB_1 species spans the entire length of the central cavity, with the acyl chain
335 remaining bound in the narrow tunnel at the occluded ER end of the cavity, and the FB_1
336 portion sitting in the wider cytoplasmic entrance (Fig. 4b and Fig. 5b-c). The newly formed
337 amide bond sits in the active site (Fig. 5c), with the carbonyl oxygen forming a hydrogen
338 bond to Tyr189 (TM3), and the amide NH hydrogen bonding to the Nε of His211 (TM4). The

339 3-hydroxyl group of FB_1, which is also present in sphingoid base substrates, forms a
340 hydrogen bond with the strictly conserved and catalytically essential Asp242 (TM5b)[17,18].
341 Such an interaction with the 3-hydroxyl group of sphingoid base substrates would optimally
342 place the sphingoid primary amine to attack the carbonyl carbon. However, further work is
343 required to investigate this hypothesis.

344 Below the active site, the cytoplasmic vestibule of the central cavity has both polar and non-
345 polar surfaces, where we noted that the hydrocarbon chain of FB_1 interacts with the long
346 hydrophobic face formed by TM5-7 (Fig. 5b,d). This hydrocarbon chain lies against the
347 conserved Trp318 of TM7 just beneath the active site. Mutation of the corresponding residue
348 in CerS5 to an alanine has been previously shown to abolish enzymatic activity[50]. In contrast,
349 introducing a phenylalanine at this position by a W318F mutation in CerS6 retained
350 approximately wild-type levels of activity (Fig. 3e). From these results, we hypothesize the
351 conserved Trp orients the sphingoid base substrate to place its amino alcohol moiety in the
352 side pocket within the active site for the second step of the reaction.

353 The face of the central cavity opposite the FB_1 hydrocarbon binding surface displays a polar
354 character, and is lined by conserved charged residues that may participate in CoA binding
355 (Fig. 5b,d). Accordingly, the positive charges provided by Lys125 and Arg131, located at the
356 cytoplasmic entrance to the cavity, adjacent to the Hox-like domain, have been previously
357 demonstrated to be important for the function of CerS5 and CerS6[20]. Furthermore, mutation
358 of Lys131 in CerS3, equivalent to CerS6's Arg131, to alanine has been implicated in
359 autosomal recessive congenital ichthyosis (ARCI)[51], a disorder of epidermal keratinization
360 which can be caused by loss of ≥ C26 ceramides due to mutations in *CERS3*[52,53].

361 The two tricarballylic acid (TCA) groups of FB_1 span the width of the cytoplasmic end of the
362 central cavity, where one of the groups interacts with Arg131 (TM2) and the other with

363 Lys328 (TM7) (Fig. 5b). Thus, through these charge-charge interactions, FB_1 links the first
364 helix of the first 3-TM bundle and the last helix of the second. Supporting the notion that FB_1
365 acts to restrain the structure, atomistic molecular dynamics (MD) simulations of covalent
366 intermediate and N-acyl FB_1-bound CerS6 monomers indicate that a bound N-palmitoyl FB_1
367 reduces the overall flexibility of the protein, including TM6, TM7, and the Hox-like domain
368 (Extended Data Fig. 9a-c). Moreover, while Lys125 is not resolved in the cryo-EM maps, in
369 our simulations Lys125 forms a salt bridge with the same TCA group that contacts Arg131
370 (Extended Data Fig. 9d). Further, the simulations show that this TCA also contacts Lys249
371 (TM5b), Tyr253 (TM5b), as well as Arg118 and Arg121 of the last helix of the Hox-like
372 domain. Therefore, FB_1 appears to mimic a number of CoA interactions through the binding
373 of one of its TCA moieties at the polar face of the cytoplasmic cavity. Finally, on the
374 opposite side of the cavity, the other TCA moiety can form salt bridges with Lys328 or
375 Arg332 (TM7) (Extended Data Fig. 9d). Overall, our cryo-EM structure and simulations
376 reveal that FB_1 is anchored by polar interactions at opposite sides of the 6TM barrel, which
377 likely hinder product release, arresting the enzyme in an inhibitory product-bound state.

378

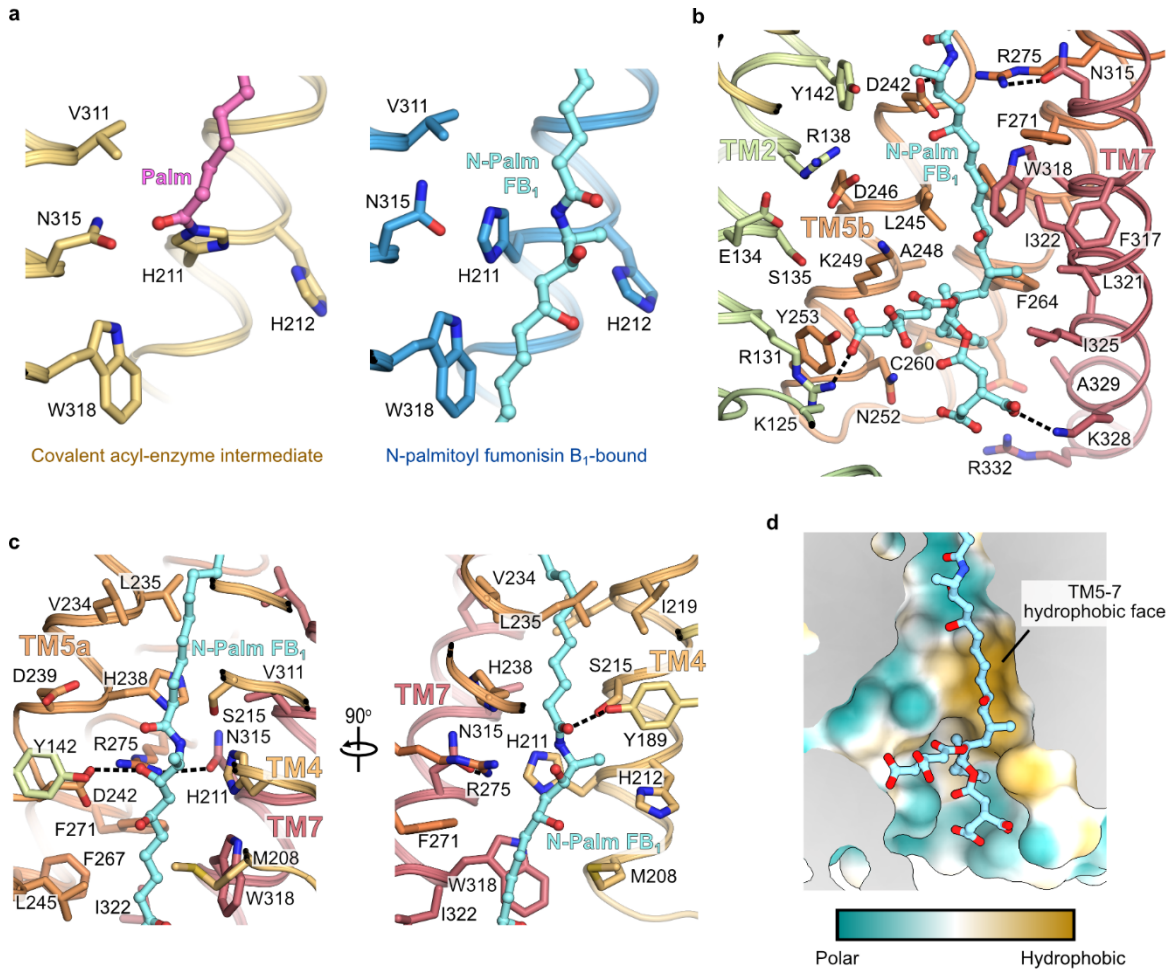

Figure 5. Binding mode of N-palmitoyl fumonisin B_1. a, Close-up view of the CerS6 active site in the covalent acyl-enzyme intermediate and N-palmitoyl FB_1-bound states, showing the transfer of the palmitoyl chain from His211 to the toxin. **b**, Cytoplasmic portion of the central cavity, viewed from the membrane plane. Residues lining the cavity are shown as sticks. Polar interactions between the carboxylates of the tricarballylic acid groups of fumonisin B_1 and positively charged residues on TM2 and TM7 are shown as dashed lines. **c**, Active site, viewed from the plane of the membrane. **d**, Polar and non-polar surfaces on the cytoplasmic half of the central cavity. Cutaway molecular surface view, showing that the hydrocarbon chain of fumonisin B_1 interacts with the large hydrophobic face formed by TM5-7.

390 **Bound lipid**

391 In examining our CerS6 cryo-EM maps, we noted both conditions clearly contain an ordered
392 non-protein density near the dimer interface, adjacent to the LH-TM1 loop and TM4 and
393 likely corresponding to a bound lipid. There, we modelled a phosphatidylcholine molecule, as
394 its head group is consistent with the shape, size and environment of the observed density
395 (Extended Data Fig. 3e). The choline head group is nestled between conserved Trp9 and
396 Trp21 in a classic aromatic box for binding quaternary amines[54]. Adjacent to the choline-
397 binding site is Trp14, which is strictly conserved in CerS2-6. Interestingly, mutation of the
398 corresponding tryptophan residue in CerS3 to an arginine has been found in patients with
399 ARCI, and the mutant protein was found to be catalytically inactive[52]. In the CerS6 structure,
400 Trp14 does not directly contact the choline head group, but it could play a structural role in
401 forming the lipid-binding site.

402

403 ## Discussion

404 Ceramide synthases carry out an essential step in sphingolipid biosynthesis and are promising
405 drug targets. Yet, our limited understanding of their structures and biochemical mechanism
406 has hindered their therapeutic targeting. Here, we provide structural snapshots of CerS6 at
407 two stages of its reaction cycle, revealing its ping-pong (double-displacement) reaction
408 mechanism which uses a histidine nucleophile that attacks the acyl-CoA thioester to form a
409 stable acyl-imidazole intermediate. This intermediate subsequently reacts with the sphingoid
410 long-chain base substrate to yield the final ceramide or dihydroceramide reaction product
411 (Fig. 6).

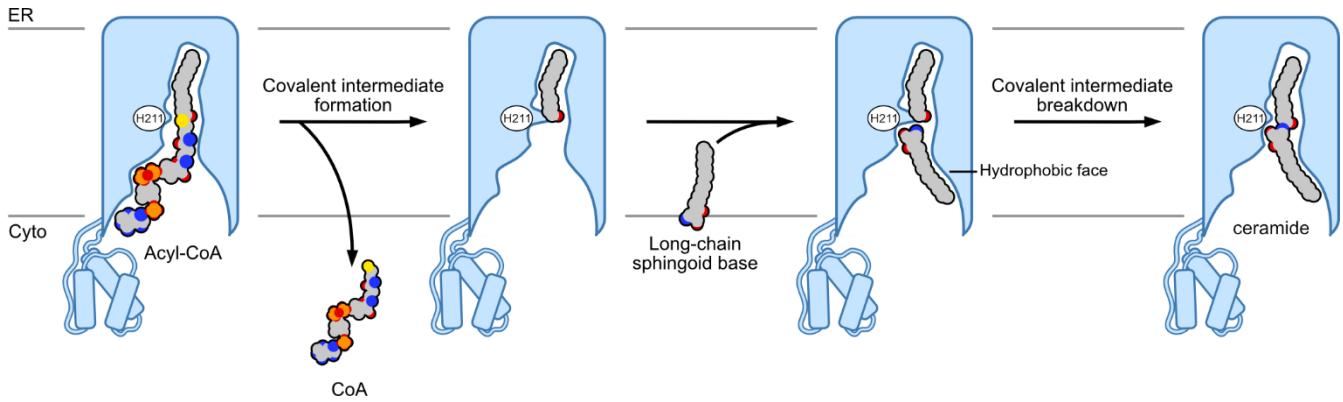

412

413 **Figure 6. Proposed double-displacement (ping-pong) mechanism of ceramide synthases.**
414 Initially, the acyl-CoA substrate binds with the acyl chain buried deep within the central tunnel and
415 the CoA moiety sitting near the cytoplasmic entrance to the central cavity. In the first step, the
416 nucleophilic attack of His211 on the acyl-CoA thioester carbonyl results in thioester cleavage,
417 covalent acyl-imidazole intermediate formation, and release of CoA. Subsequently, the long-chain
418 sphingoid base substrate binds, with its hydrocarbon chain interacting with the hydrophobic face of
419 the central cavity and its amino alcohol moiety sitting in the side pocket in the active site. In the
420 second step of the reaction, the primary amine of the long-chain base attacks the acyl-imidazole
421 intermediate, leading to covalent intermediate breakdown and formation of the final N-acyl
422 sphingoid base (ceramide) product.

423

424 Although CoA and the hydrocarbon chain of long-chain bases likely interact at distinct faces
425 of the cytoplasmic vestibule, there is not enough space for the acyl-CoA and long-chain base
426 substrates to bind at the same time. Therefore, upon thioester cleavage and covalent
427 intermediate formation, the CoA product needs to exit the central cavity before the long-chain
428 base substrate can bind. We hypothesize that the amino alcohol group of the long-chain base
429 would bind in a discrete side pocket lined by polar residues conserved across the entire CerS
430 family. This long-chain base is further oriented for the second step of the reaction by
431 hydrophobic residues located at the entrance to this pocket, particularly by the conserved
432 Trp318 (TM7). The primary amine of the long-chain base then attacks the acyl-enzyme
433 intermediate to form the final reaction product. Release of this product into the membrane

434 likely occurs between two transmembrane helices, and the two halves of the 6TM barrel
435 immediately suggest an egress route between TM4 and TM7. Indeed, we found that the TCA
436 groups of N-palmitoyl FB_1 attach to both halves of the barrel and restrict the movement of
437 TM7, suggesting these interactions likely prevent that product's release. Indeed, this
438 proposed role for the TCA groups of FB_1 is consistent with previous reports that the
439 hydrolysed form of FB_1, lacking the TCA moieties, is a weaker CerS inhibitor[55]. However,
440 FB_1 is competitive towards both substrates[30]. This suggests FB_1's mode of inhibition of CerS
441 is likely to be multifaceted, sterically blocking substrate binding to the apo state, and locking
442 the protein in a product bound state as shown here.

443 Recently, Zelnik et al. postulated that CerS2, and ceramide synthases more generally, use a
444 ternary complex reaction mechanism[50]. In this model, the substrates bind orthogonally, and
445 the long-chain base would access the active site through a side entrance located near the
446 membrane mid-point, where it would bind parallel to the membrane plane. This proposed
447 substrate-binding arrangement is similar to that of small-molecule membrane-bound O-
448 acyltransferases (MBOATs) and led to the suggestion that CerS may catalyze the direct
449 transfer of the acyl chain from acyl-CoA to the long-chain base in a single step involving the
450 two active site histidines[50]. In addition, while this manuscript was under review, the cryo-EM
451 structure of yeast Lac1p bound to an acyl-CoA was reported. That structure revealed a small
452 lateral opening in Lac1p adjacent to the active site[56]. This observation led the authors to
453 hypothesize that it could potentially correspond to the entry route for sphingoid base
454 substrates[56]. However, this lateral opening is not present in our cryo-EM structures of CerS6
455 or in our molecular dynamics simulations. Instead, our experimental structures and
456 biochemical studies of CerS6 present several pieces of evidence which support a ping-pong
457 type mechanism, and challenge a ternary complex reaction. First, CerS possess a completely
458 different fold to that of the MBOATs. Indeed, CerS6's structure is strikingly similar to the

459 fatty acid elongase ELOVL7, forming a 6-TM barrel that encloses a narrow tunnel with an
460 essential and structurally superimposable active site histidine pair, which we have also
461 recently shown to catalyze acyl chain transfer via a ping-pong reaction mechanism[34]. Further,
462 purification of a stable acyl-CerS6 adduct species is incompatible with a ternary complex
463 reaction mechanism. Rather, by incubating acyl-CerS6 with sphinganine, FB_1 or FTY720, we
464 show that this species is a *bona fide* reaction intermediate which results in the expected
465 product upon exposure to the second substrate. Additionally, we captured the product-bound
466 state in the N-acyl FB_1-bound structure, where the toxin's hydrocarbon chain binds
467 perpendicularly to the membrane plane and interacts with the hydrophobic face of the central
468 cavity formed by TM5-7. This binding mode in the N-acyl FB_1-bound structure conflicts with
469 a MBOAT-style substrate coordination, but is still consistent with the action of CerS on the
470 fluorescently labelled NBD-sphinganine[57] as the bulky NBD moiety would sit near the wide
471 cytoplasmic entrance of the central cavity. Crucially, FB_1 is a structural analog of
472 sphinganine which undergoes N-acylation similarly to sphingoid base substrates, and its
473 mode of inhibition is competitive towards sphinganine[30], implying that FB_1 and sphinganine
474 likely bind to CerS in a similar manner. In aggregate, our data do not support a ternary
475 complex reaction mechanism. Rather, an ELOVL-type ping-pong model is consistent with
476 both our newly determined structures and biochemical results, and previously reported CerS
477 mutants[17,18,47].

478 Our observation that CerS6 can transfer a C16:0 acyl chain to the primary amine of FTY720
479 has important consequences for using compounds that mimic sphingoid bases in a clinical
480 setting. The action of CerS partially explains the N-acylated FTY720 species found during
481 the FTY720 drug trials[40], and by extension this enzyme family may play a role in the
482 pharmacokinetics of other sphingoid analogs. Further, our FB_1 results reveal how this toxin
483 can arrest the protein in a product-bound state (Extended Data Fig. 10), supporting the notion

484 that unintended substrates of this enzyme family may result in the formation of inhibitory
485 products. Taking advantage of this inhibition, ceramide or N-acyl FB_1 mimetics could
486 provide novel chemical scaffolds for new CerS inhibitors.

487 # Methods

488 ## CerS6 cloning and expression

489 The *Homo sapiens CERS6* gene, encoding the CerS6 protein (Uniprot ID Q6ZMG9) was
490 cloned into the baculovirus transfer vector pHTBV1.1-CT10H-SIII-LIC (adapted from the
491 BacMam vector pHTBV1.1, provided by Frederick Boyce, Massachusetts General Hospital,
492 Cambridge, MA) upstream of C-terminal TEV-cleavable 10x His and Twin-Strep tags. The
493 construct used for structural determination lacked the final 42 amino acids, which are
494 predicted to be disordered. For *in vitro* biotinylation, the avi-tagged CerS6 construct
495 contained a GGGS linker between CerS6 and the Avi tag (GLNDIFEAQKIE), located
496 upstream of the TEV cleavage site. Site-directed mutagenesis was performed using the Q5
497 site-directed mutagenesis kit (NEB).

498 Baculoviral DNA was generated by transposition of DH10Bac with the baculovirus transfer
499 vector. Baculovirus was produced by transfecting *Sf*9 cells (Thermo Fisher Scientific) with
500 the baculoviral DNA using the Insect GeneJuice transfection reagent (Merck Milipore). The
501 virus was amplified by infecting *Sf*9 cells in the presence of 2 % fetal bovine serum and
502 incubating for 72h at 27 ºC. For large-scale protein expression in Expi293F GnTI- cells
503 (Thermo Fisher Scientific) in Freestyle 293 expression medium (Thermo Fisher Scientific),
504 cells were transduced with baculovirus and supplemented with 5 mM sodium butyrate. Cells
505 were incubated in a humidity-controlled orbital shaker at 37 ºC with 8 % CO_2 for 48h, and
506 subsequently harvested by centrifugation at 900 x g for 15 min. Pelleted cells were washed
507 with phosphate buffered saline (PBS), pelleted again by centrifugation, flash-frozen in liquid
508 N_2 and stored at -80 ºC. To compare mutant activity, wild-type and mutant proteins were
509 expressed in Expi293F cells (Thermo Fisher Scientific) using the same protocol.

510

511 **Large-scale CerS6 purification**

512 CerS6-overexpressing cells were re-suspended in Buffer A (50 mM HEPES pH 7.5, 200 mM
513 NaCl, 5 % (v/v) glycerol) and solubilized with 1 % (w/v) lauryl maltose neopentyl glycol
514 (LMNG) (Anatrace) and 0.1 % (w/v) cholesteryl hemisuccinate (CHS) (Sigma-Aldrich).
515 Insoluble material was removed by centrifugation at 35,000 x g, and the protein was purified
516 from the supernatant by batch binding to Strep-Tactin XT Superflow resin (IBA
517 Lifesciences). The resin was washed initially with Buffer A containing 0.05 % (w/v) GDN,
518 and subsequently with Buffer A supplemented with 1 mM ATP (Sigma-Aldrich), 10 mM
519 $MgCl_2$, and 0.05 % (w/v) GDN. CerS6 was eluted from the resin using Buffer A
520 supplemented with 100 mM D-biotin (Fluorochem) and 0.02 % (w/v) GDN, and the C-
521 terminal tag was cleaved by TEV protease digestion overnight. The His-tagged TEV protease
522 was removed by binding to Co^{2+}-charged TALON resin (Clontech) and the flow-through
523 concentrated using a 100 kDa molecular weight cut off concentrator (Corning). The protein
524 was finally purified by size-exclusion chromatography on a Superdex 200 Increase 10/300
525 GL column (GE Healthcare), pre-equilibrated in SEC buffer (20 mM HEPES pH 7.5, 200
526 mM NaCl, and 0.01 % (w/v) GDN).

527 For nanobody generation and selection, GDN was replaced in the purification buffers with
528 0.003 % (w/v) LMNG and 0.0003 % (w/v) CHS. For *in vitro* biotinylation of C-terminally
529 avi-tagged CerS6, during the TEV cleavage step, the protein sample was further
530 supplemented with 15 mM $MgCl_2$, 15 mM ATP, 50 mM bicine pH 8.3, and BirA at a 1:15
531 (w/w) BirA:CerS ratio. Biotinylation efficiency was routinely monitored by denaturing intact
532 protein mass spectrometry.

533 For structural determination, CerS6 was mixed with a 1.5 x molar excess of nanobody Nb22
534 and incubated for 1h on ice. The CerS6-Nb22 complex was purified by size-exclusion

535 chromatography, concentrated to 5 mg mL^{-1} using a 100 kDa molecular weight cut off
536 concentrator (Sartorius), and processed immediately for cryo-electron microscopy.

537

538 **Nanobody library generation and selection**

539 Purified CerS6 was reconstituted at a 1:20 (protein:lipid (w/w) ratio into liposomes composed
540 of POPC:POPG:DMPC:DMPG (7:3:7:3 (w/w)) as previously described[58].

541 To obtain anti-CerS6 nanobodies, alpacas were immunized and the nanobody library was
542 generated as previously described[59], with the exception that 200 µg purified CerS6 in
543 proteoliposomes were used for each immunization. All the procedures concerning alpaca
544 immunization were approved by the Cantonal Veterinary Office of Zurich, Switzerland
545 (License No. ZH 198/17). The resulting nanobody library was screened by biopanning
546 against CerS6. Subsequently, 190 single clones from the enriched nanobody library were
547 analyzed by ELISA for binding to CerS6. 96 ELISA-positive clones were Sanger sequenced
548 and grouped in families according to their CDR length and sequence diversity[60]. Of these, 42
549 unique nanobodies were identified as belonging to 26 nanobody families and were taken for
550 further validation.

551 Nanobodies were expressed in 50 mL scale in WK6 cells and purified from periplasmic
552 extracts using Ni^{2+}-NTA resin, as previously described[60]. Unique nanobodies were screened
553 by biolayer interferometry (BLI) in an Octet Red 384 system (Sartorius) using Streptavidin
554 SA biosensors (Sartorius) loaded with 40 µg mL^{-1} biotinylated CerS6 in SEC buffer
555 containing 0.003 % (w/v) LMNG, 0.0003 % (w/v) CHS. Nanobodies with slow off rates were
556 identified, and nanobody-22 was prioritized for structural studies.

557

558 **Thermal stability measurements**

559 Thermal unfolding experiments were carried out on a Prometheus NT.48 instrument
560 (NanoTemper Technologies) using 5 µM CerS6 solubilized in 0.003% LMNG and 0.0003%
561 CHS. The protein was incubated for 1h at 4 ºC in the presence or absence of 20 or 100 µM
562 FTY720 (Sigma-Aldrich) or fumonisin B_1 (Sigma-Aldrich). Proteins were heated from 20 ºC
563 to 95 ºC, at a rate of 1 ºC min^{-1}, and unfolding was monitored by the ratio of fluorescence
564 emission at 350 nm and 330 nm. The melting temperature was determined from the inflection
565 point of the transition using the PR.ThermControl software (NanoTemper Technologies).

566

567 **Cryo-EM sample preparation and data acquisition**

568 The purified CerS6-Nb22 complex (5 mg mL^{-1}) was applied to freshly glow-discharged
569 Quantifoil 200 mesh Au R1.2/1.3 grids. Plunge freezing in liquid ethane was carried out
570 using a Vitrobot Mark IV (Thermo Fisher Scientific) set to 4 ºC and 100 % humidity. For the
571 CerS6-Nb22-FB_1 complex, the SEC-purified CerS6-Nb22 complex was incubated with 120
572 µM fumonisin B_1 (Sigma-Aldrich) for 10 minutes on ice prior to protein concentration and
573 subsequently for an additional 2h on ice prior to grid preparation. EM grids were screened on
574 a Glacios (OPIC, Oxford) and high resolution data were collected on a Titan Krios G3
575 microscope (LISCB, University of Leicester) operating at 300 kV and equipped with a
576 Bioquantum Energy Filter (Gatan) (operated at 20 eV slit width) and a K3 direct electron
577 detector (Gatan) at 130,000 x nominal magnification, in super-resolution mode (2x binning;
578 physical pixel size: 0.656 Å px^{-1}), using a defocus range between -0.8 µm and -2.4 µm. The
579 total exposure dose was 56.3 e^{-} $Å^{-2}$, fractionated over 50 frames. In total, 14,309 and 18,386
580 movies were collected for the CerS6-Nb22 and CerS6-Nb22-FB_1 datasets, respectively.

581

582 **Cryo-EM data processing and model building**

583 Movies were motion-corrected using MotionCor2[61], and CTF estimation was carried out in
584 cryoSPARC[62] (version 3.3.1). Micrographs with bad CTF fitting (>5 Å) were excluded,
585 yielding 14,196 and 16,647 micrographs for further analysis for the CerS6-Nb22 and for the
586 CerS6-Nb22-FB_1 datasets, respectively.

587 For the covalent acyl-enzyme intermediate dataset, particles were initially blob picked and
588 extracted from a subset of micrographs, and representative well-resolved 2D classes were
589 used for template-based picking of the entire dataset. 3,400,118 template-picked particles
590 were extracted in a 360 px box Fourier cropped to 120 px corresponding to a pixel size of
591 1.968 Å px^{-1} and classified in two rounds of reference-free 2D classification yielding
592 1,261,928 good particles. Four a*b-initio* models were generated and used as reference models
593 in heterogeneous refinement. Particles belonging to the well-resolved 2:2 CerS6-Nb dimer
594 complex class (53 % of input particles) were selected and subjected to a further round of
595 heterogeneous refinement. The best resolved set of particles (497,504) were then subjected to
596 non-uniform refinement[63] with C2 symmetry imposed, yielding a 3.21 Å reconstruction
597 (FSC = 0.143). These aligned particles were imported into RELION using the csparc2star.py
598 script from the UCSF pyem package[64] and re-extracted in a 360 px box Fourier cropped to
599 270 px, corresponding to a pixel size of 0.875 Å px^{-1}. In RELION, CTF parameters were
600 refined, followed by Bayesian particle polishing[65]. The polished particles were subjected to
601 3D classification without image alignment (k =10, T=12). Certain classes displayed worse
602 side-chain density and local deviations from C2 symmetry. Therefore, to improve map
603 quality, the 93,680 particles belonging to the two highest-resolution C2-symmetric classes
604 were re-imported into cryoSPARC, and subjected to a final non-uniform refinement with C2
605 symmetry, yielding a 3.22 Å reconstruction (FSC = 0.143). Importantly, even though CTF
606 refinement, Bayesian polishing and 3D classification in RELION did not improve the

607 nominal resolution, the final reconstruction reveals better defined features, including
608 improved side-chain density in the CerS6 active site (Extended Data Fig. 2f,g).

609 The N-acyl FB_1 dataset was processed using the same workflow as the covalent acyl-enzyme
610 intermediate dataset, with the following changes. 3,998,935 template-picked particles were
611 classified in two rounds of reference-free 2D classification, yielding 1,353,329 good
612 particles. Four a*b-initio* models were generated and used as reference models in
613 heterogeneous refinement. 641,462 particles belonging to the well-resolved 2:2 CerS6-Nb
614 dimer complex class (48 % of input particles) were subjected to non-uniform refinement with
615 C2 symmetry imposed, yielding a 3.17 Å reconstruction. After CTF refinement, Bayesian
616 polishing and 3D classification without image alignment in RELION, the 154,239 particles
617 belonging to the three highest-resolution C2-symmetric classes were selected. These particles
618 were re-imported into cryoSPARC, and subjected to a final non-uniform refinement with C2
619 symmetry, yielding a 2.95 Å reconstruction (FSC = 0.143).

620 Atomic models were generated by fitting the CerS6 AlphaFold2[66] prediction and a Phyre2[67]
621 nanobody homology model into the cryo-EM maps, and subsequently manually adjusted in
622 Coot[68]. In both datasets, residues 72-119, corresponding to the Hox-like domains, were
623 poorly resolved in the sharpened maps. However, their position is evident in unsharpened and
624 blurred maps (Extended Data Fig. 2e; Extended Data Fig. 3a). In order to model this region,
625 we used tight restraints to the Alphafold2 prediction for this domain and docked it into the
626 envelope of the blurred maps (B_{Blur} = 200 $Å^2$), and surface-exposed side-chains were
627 truncated at Cβ. The atomic models were refined using PHENIX real-space refinement[69] with
628 secondary structure and Ramachandran restraints, and NCS constraints. Restraint dictionaries
629 for FB_1 and the covalently attached C16:0 chain were generated using AceDRG[70]. The final
630 models comprise residues 2-330 (covalent intermediate state) or 2-334 (N-palmitoyl FB_1-
631 bound state) of CerS6, residues 1-124 of nanobody-22, the C16:0 chain covalently attached to

632 His211 of CerS6 or the N-palmitoyl FB_1 product, one phosphatidylcholine molecule and the
633 first N-acetylglucosamine residue of the N-linked glycan visible on Asn18. Weighted Fo −
634 Fc ligand difference maps were calculated using Servalcat [71], available in CCPEM[72], by
635 omitting the ligands from the atomic models.

636

637 **Denaturing intact protein mass spectrometry**

638 The intact masses of purified protein samples were analyzed by denaturing intact protein
639 mass spectrometry, conducted using an Agilent 1290 Infinity LC system in line with an
640 Agilent 6530 Accurate-Mass quadrupole time-of-flight mass spectrometer (Agilent
641 Technologies), as previously described[34]. Typically, 5-8 µg of purified protein (at 1.5-2.0 mg
642 mL^{-1}), diluted to 20 µL in 30 % methanol in 0.1 % formic acid, were used per injection. Data
643 were acquired between 100-3200 *m/z* and analyzed using MassHunter Qualitative Analysis
644 v.B.07.00 (Agilent Technologies) software. Peaks between 650-3200 *m/z* in the sum of the
645 mass spectra obtained during protein elution were deconvoluted using the maximum entropy
646 charge deconvolution algorithm.

647 The identity of the deconvoluted mass peaks was assigned initially based on the expected
648 mass of the purified proteins, and subsequently based on the observed mass shifts between
649 peaks in the deconvoluted mass spectra. The lower molecular weight CerS6 peak corresponds
650 to loss of the initiator methionine (theoretical mass shift of -131.20 Da), acetylation of the
651 new N-terminus (theoretical: +42.04 Da) and addition of an N-linked GlcNAc (theoretical:
652 +203.19 Da). However, the major glycosylation species observed contains the complete core
653 N-linked glycan (theoretical: +1217.05 Da), as expected for protein expressed in Expi293F
654 GnTI- cells. In addition, we observed +237.47 and +238.51 Da mass shifts relatively to these
655 two glycosylated species, respectively, which we interpreted as palmitoylation at a single site

656 (theoretical: +238.41 Da), corresponding to the covalent acyl-imidazole intermediate
657 observed in the cryo-EM structure. One additional modification was observed (~ +264 Da),
658 but its identity could not be assigned. This unknown modification occurs at a distinct site to
659 that of the palmitoylation, as both modifications can occur simultaneously in the same protein
660 molecule (Extended Data Fig. 1f,g), thus excluding the possibility of this unknown
661 modification occurring in the active site.

662 To monitor the reaction of the covalent intermediate species with the second substrates, prior
663 to denaturing intact protein mass spectrometry analysis the protein (2 mg mL^{-1}) was
664 incubated with 200 µM sphinganine (Avanti Polar Lipids), 200 µM fumonisin B_1 (Sigma-
665 Aldrich), or 600 µM FTY720 (Sigma-Aldrich) for 1h 30 min at 37 ºC. All intact mass
666 experiments were conducted at least twice using distinct biological samples. Replicate
667 deconvoluted mass spectra are shown in Extended Data Fig. 5.

668

669 **Product detection by liquid chromatography high-resolution mass spectrometry (LC-**
670 **HRMS)**

671 Product detection by LC-HRMS was conducted on a nanoElute LC system in line with a
672 TIMS TOF Pro 2 mass spectrometer (Bruker). The reactions were set up as described for the
673 denaturing intact protein MS experiments, diluted 1:40 (v/v) in 30 % methanol in 0.1 %
674 formic acid, and 1 µL of each sample was injected onto an IonOpticks C18 nano UHPLC
675 column (1.6 µm particle size; 0.075 x 250 mm).

676 The flow rate was set to 0.5 µL min^{-1}, and the solvent system consisted of 0.1 % Optima LC–
677 MS grade formic acid (Fisher Chemical) in high-performance liquid chromatography
678 electrochemical grade water (Fisher Chemical) (solvent A) and 0.1 % formic acid in Optima
679 LC–MS grade methanol (Fisher Chemical) (solvent B). Initial conditions were 60 % solvent

680 B, and a linear gradient from 60 % to 95 % solvent B was applied over 17.8 min to elute the
681 samples. This was then followed by a final 2.2 min isocratic elution with 95 % solvent B,
682 before the system was re-equilibrated between samples for 5 min with 60 % solvent B.

683 The mass spectrometer was operated in positive ion mode with a capillary voltage of 1,600
684 V, and the drying gas was supplied at 180 ºC with a flow rate of 3 L $min^{-}1$. Additional
685 parameters were: deflection 1 delta of 70 V, funnel 1 RF of 350 Vpp, funnel 2 RF of 600
686 Vpp, multipole RF of 500 Vpp. Data were acquired between 150-2200 *m/z*, and analyzed
687 using the Bruker Compass DataAnalysis 5.3.556 software. The extracted ion chromatograms
688 are presented in Fig. 3c and Fig. 4d, and correspond to the theoretical $[M+H]^+$ ions
689 (tolerance: ± 0.005 *m/z*) of the reaction products N-palmitoyl dihydrosphingosine (C16:0
690 ceramide) (theoretical *m/z*: 540.5350), N-palmitoyl FB_1 (theoretical *m/z*: 960.6254), and N-
691 palmitoyl FTY720 (theoretical *m/z*: 546.4881).

692

693 **Liquid chromatography electrospray ionization tandem mass spectrometry (LC-ESI-**
694 **MS/MS) characterization of N-palmitoyl FTY720**

695 To structurally characterize the proposed N-palmitoyl FTY720 reaction product, purified
696 protein was incubated with 600 µM FTY720 as before, and the reaction mixture was initially
697 analyzed by LC-ESI-MS on an Agilent 1290 Infinity LC System in line with an Agilent 6530
698 Accurate-Mass quadrupole time-of-flight mass spectrometer (Agilent Technologies) as
699 described above. This enabled the identification of the putative $[M+H]^+$ ion of the N-
700 palmitoyl FTY720 product (observed *m/z*: 546.4849; theoretical *m/z*: 546.4881). Its product
701 ion spectrum was then obtained by LC-ESI-MS/MS. For this purpose, the mass spectrometer
702 was operated in positive electrospray ionization (ESI+), 4 GHz mode. MS parameters were
703 capillary voltage of 4,000 V, fragmentor voltage of 175 V. Data were acquired between 100-

704 1700 *m/z*. The targeted parent ion (546.4881 *m/z*; retention time = 8.713 min) was fragmented
705 using a collision energy of 14 V.

706

707 **Dihydroceramide synthase activity measurements**

708 For activity assays, wild-type or mutant CerS6 proteins were over-expressed in Expi293F
709 cells, and membranes were prepared as follows. Cell pellet from 0.5 L of culture was thawed
710 in PBS, lysed using an Emulsiflex C5 homogeniser (Avestin), and cell debris was removed
711 by centrifugation. Membranes were subsequently isolated by ultracentrifugation at 160,000 x
712 g for 1h 30 min, resuspended in Assay Buffer (20 mM HEPES pH 7.5, 25 mM KCl, 1 mM
713 $MgSO_4$, 0.1 % (v/v) glycerol), flash-frozen in liquid N_2 and stored at -80 ºC.

714 On the day of the assay, membranes were thawed, diluted to 0.25 mg mL^{-1}, and 20 µL of
715 diluted membranes were dispensed per well on flat bottom polystyrene 384-well Lumitrac
716 plates (Greiner Bio One). Then, 50 µM sphinganine (2.5 µL 500 µM sphinganine in Assay
717 Buffer containing 10% ethanol) and 50 µM palmitoyl-CoA (Sigma-Aldrich) (2.5 µL 500 µM
718 palmitoyl-CoA in Assay Buffer) were added to each well for a final reaction volume of 25
719 µL. For untreated controls, 5 µL of Assay Buffer were added instead of the substrates. The
720 plates were then incubated for 1h at room temperature, and the reaction was terminated by the
721 addition of 40 µL butanol spiked with N-palmitoyl(d9) dihydrosphingosine (Avanti Polar
722 Lipids) to yield a final concentration of 5 µM N-palmitoyl(d9) dihydrosphingosine as an
723 internal standard. The plates were then shaken at 1,800 rpm for 2 min, centrifuged at 1,000 x
724 g for 30 s, and 40 µL of the organic (upper) phase were transferred into 384-well
725 polypropylene deep well plates (Greiner Bio One) and diluted with 40 µL butanol.

726 The analytical sample handling was performed by a rapid-injecting RapidFire autosampler
727 system (Agilent, Waldbronn, Germany) coupled to a triple quadrupole mass spectrometer

728 (Triple Quad 6500, AB Sciex Germany GmbH, Darmstadt, Germany) as previously
729 described[73], with the following modifications. Liquid sample is aspirated by a vacuum pump
730 into a 10 µL sample loop for 6000 ms and subsequently flushed for 3000 ms onto a C4
731 cartridge (Agilent) with the aqueous mobile phase (99.5% water, 0.49% acetic Acid, 0.01%
732 Trifluoroacetic acid, flow rate 1.5 mL min^{-1}). The MRM transition for C16:0
733 dihydroceramide is 540.5 → 266.3 *m/z* (declustering potential 130V, collision energy 38 V)
734 and for the internal standard C16:0 (d9)dihydroceramide is 549.5 → 266.3 *m/z* (declustering
735 potential 130V, collision energy 38 V). The mass spectrometer was operated in positive
736 ionization mode (curtain gas 35 a.u., collision gas medium, ion spray voltage 4200 V,
737 temperature 550 °C, ion source gas 1 65 a.u., ion source gas 2 80 a.u.). MS data processing
738 was performed in GMSU (Alpharetta, GA, USA), and peak area ratios between C16:0
739 dihydroceramide and internal standard peaks were calculated.

740 Expression of each mutant in the membrane samples was evaluated through western blotting
741 using 10 ng mL^{-1} Strep-Tactin conjugated with horseradish peroxidase (IBA Lifesciences)
742 and using SYPRO Ruby (Thermo Fisher Scientific) staining as a loading control (Source
743 Data Fig. 1). Band intensity was quantified using the GeneTools software (Syngene) and
744 activity was normalized to protein expression.

745

746 **Molecular dynamics simulations**

747 Atomistic molecular dynamics simulations were performed using the Desmond software
748 package (D. E. Shaw Research, New York, NY) within the Maestro software suite
749 (Schrödinger). The simulation setup and analysis were carried out as follows: For each of the
750 two states, a CerS6 monomer was embedded in a lipid bilayer consisting of 99 POPC
751 molecules after undergoing the protein preparation step as implemented in Maestro. The

752 dimensions of the simulation cell were approximately 90x70x70 Å, with a minimum distance
753 of 10 Å between the protein and the cell boundaries. The systems contained 8,855 (covalent
754 intermediate bound state) or 9,368 (N-acyl FB1 bound state) water molecules and
755 correspondingly 8 or 6 chloride counterions to maintain overall charge neutrality. The
756 simulations were performed using the OPLS4 force field[74] for the protein and lipid
757 molecules, and the SPC water model for the water molecules. The system was set up using
758 the Maestro software suite (Schrödinger). The simulations were run in Desmond using an
759 NPT ensemble at a temperature of 300K. A timestep of 2 fs was employed for the integration
760 of equations of motion. Four independent simulations were performed, each with a duration
761 of 100 ns, resulting in a total simulation time of 400 ns. Snapshots of the system were
762 recorded every 100 ps for further analysis.

763 **Figures**

764 Figures depicting molecular models were generated using PyMOL[75] and ChimeraX[76].

765 **Data availability**

766 The cryo-EM maps have been deposited in the Electron Microscopy Data Bank (EMDB)
767 under accession codes EMD-18770 (covalent acyl-enzyme intermediate state) and EMD-
768 18771 (N-acyl FB_1-bound state). The atomic models have been deposited in the Protein Data
769 Bank under accession codes 8QZ6 (covalent acyl-enzyme intermediate state) and 8QZ7 (N-
770 acyl FB_1-bound state).

771

772 **Acknowledgements**

773 T.C.P. was supported by a Wellcome PhD studentship (102164/B/15/Z). Initial work on this
774 project was funded by the Structural Genomics Consortium, a registered charity (number
775 1097737) that received funds from AbbVie, Bayer, Boehringer Ingelheim, the Canada
776 Foundation for Innovation, Genome Canada, Janssen, Merck, Novartis, the Ontario Ministry
777 of Economic Development and Innovation, Pfizer, and Takeda, as well as the Wellcome
778 Trust (106169/Z/14/Z). D.B.S., A.C.W.P. and G.C. were supported by the Innovative
779 Medicines Initiative 2 Joint Undertaking (JU) under grant agreement No 875510. The JU
780 receives support from the European Union's Horizon 2020 research and innovation program
781 and EFPIA and Ontario Institute for Cancer Research, Royal Institution for the Advancement
782 of Learning McGill University, Kungliga Tekniska Hoegskolan, Diamond Light Source
783 Limited. Electron microscopy was provided through the Oxford Particle Imaging Centre
784 (OPIC), an Instruct-ERIC centre (funded by Wellcome Trust JIF award [060208/Z/00/Z] and
785 equipment grant [093305/Z/10/Z]) and the Midlands Regional CryoEM Facility at the
786 Leicester Institute of Structural and Chemical Biology (LISCB), major funding from MRC
787 (MC_PC_17136). We thank Christos S. Savva (LISCB) for technical assistance with cryo-

EM data collection and William Greenland (Agilent) for technical advice on tandem mass spectrometry. We thank Wyatt Yue and Christian Siebold for helpful discussions.

Author contributions

T.C.P. expressed and purified protein samples, prepared proteoliposome samples for alpaca immunization and membranes for mutant activity testing, carried out biophysical characterizations including bio-layer interferometry experiments, designed and generated CerS6 mutants by site-directed mutagenesis, built and refined the atomic models, and performed intact protein MS, product identification by high-resolution MS and small-molecule structural characterization by LC-ESI-MS/MS. T.C.P. and G.C. prepared cryo-EM grids. T.C.P. and A.C.W.P. collected and processed the cryo-EM data. C.S.T. carried out the molecular dynamics simulations and analysis. A.Q. was involved in the early stages of the project, including initial screening of expression and purification conditions. R.C. provided access to mass spectrometry instruments for intact protein and small-molecule analysis, and assisted with small-molecule MS experiments. S.Š. conducted alpaca immunizations, nanobody library generation, panning and identification of unique nanobody sequences. M.T. performed the CerS6 mutant activity assays, supervised by S.T.. T.C.P. and D.B.S. wrote the original draft of the manuscript. All authors participated in the discussion and manuscript editing. A.P., E.P.C., G.S. and D.B.S. supervised the research.

Competing interests

The authors declare no competing interests. C.S.T., M.T., S.T., A.P., and G.S. are employees of Boehringer Ingelheim Pharma GmbH & Co. KG.

811 **References**

812 1 Summers, S. A., Chaurasia, B. & Holland, W. L. Metabolic Messengers: ceramides. *Nature*
813 *Metabolism* **1**, 1051-1058, doi:10.1038/s42255-019-0134-8 (2019).
814 2 Turpin, S. M. *et al.* Obesity-induced CerS6-dependent C16:0 ceramide production promotes
815 weight gain and glucose intolerance. *Cell Metab* **20**, 678-686,
816 doi:10.1016/j.cmet.2014.08.002 (2014).
817 3 Apostolopoulou, M. *et al.* Specific Hepatic Sphingolipids Relate to Insulin Resistance,
818 Oxidative Stress, and Inflammation in Nonalcoholic Steatohepatitis. *Diabetes Care* **41**, 1235-
819 1243, doi:10.2337/dc17-1318 (2018).
820 4 Hajduch, E., Lachkar, F., Ferre, P. & Foufelle, F. Roles of Ceramides in Non-Alcoholic Fatty
821 Liver Disease. *J Clin Med* **10**, 792, doi:10.3390/jcm10040792 (2021).
822 5 Hammerschmidt, P. & Brüning, J. C. Contribution of specific ceramides to obesity-associated
823 metabolic diseases. *Cell Mol Life Sci* **79**, 395, doi:10.1007/s00018-022-04401-3 (2022).
824 6 Neeland, I. J. *et al.* Relation of plasma ceramides to visceral adiposity, insulin resistance and
825 the development of type 2 diabetes mellitus: the Dallas Heart Study. *Diabetologia* **61**, 2570-
826 2579, doi:10.1007/s00125-018-4720-1 (2018).
827 7 Błachnio-Zabielska, A. U. *et al.* Increased bioactive lipids content in human subcutaneous
828 and epicardial fat tissue correlates with insulin resistance. *Lipids* **47**, 1131-1141,
829 doi:10.1007/s11745-012-3722-x (2012).
830 8 Luukkonen, P. K. *et al.* Hepatic ceramides dissociate steatosis and insulin resistance in
831 patients with non-alcoholic fatty liver disease. *J Hepatol* **64**, 1167-1175,
832 doi:10.1016/j.jhep.2016.01.002 (2016).
833 9 Levy, M. & Futerman, A. H. Mammalian ceramide synthases. *IUBMB Life* **62**, 347-356,
834 doi:10.1002/iub.319 (2010).
835 10 Ternes, P., Franke, S., Zähringer, U., Sperling, P. & Heinz, E. Identification and
836 characterization of a sphingolipid delta 4-desaturase family. *J Biol Chem* **277**, 25512-25518,
837 doi:10.1074/jbc.M202947200 (2002).
838 11 Kitatani, K., Idkowiak-Baldys, J. & Hannun, Y. A. The sphingolipid salvage pathway in
839 ceramide metabolism and signaling. *Cell Signal* **20**, 1010-1018,
840 doi:10.1016/j.cellsig.2007.12.006 (2008).
841 12 Raichur, S. *et al.* The role of C16:0 ceramide in the development of obesity and type 2
842 diabetes: CerS6 inhibition as a novel therapeutic approach. *Mol Metab* **21**, 36-50,
843 doi:10.1016/j.molmet.2018.12.008 (2019).
844 13 Raichur, S. Ceramide Synthases Are Attractive Drug Targets for Treating Metabolic Diseases.
845 *Front Endocrinol* **11**, 483, doi:10.3389/fendo.2020.00483 (2020).
846 14 Hammerschmidt, P. *et al.* CerS6-Derived Sphingolipids Interact with Mff and Promote
847 Mitochondrial Fragmentation in Obesity. *Cell* **177**, 1536-1552.e1523,
848 doi:10.1016/j.cell.2019.05.008 (2019).
849 15 Mizutani, Y., Kihara, A. & Igarashi, Y. Mammalian Lass6 and its related family members
850 regulate synthesis of specific ceramides. *Biochemical Journal* **390**, 263-271,
851 doi:10.1042/bj20050291 (2005).
852 16 Winter, E. & Ponting, C. P. TRAM, LAG1 and CLN8: members of a novel family of lipid-sensing
853 domains? *Trends Biochem Sci* **27**, 381-383, doi:10.1016/s0968-0004(02)02154-0 (2002).
854 17 Spassieva, S. *et al.* Necessary role for the Lag1p motif in (dihydro)ceramide synthase activity.
855 *J Biol Chem* **281**, 33931-33938, doi:10.1074/jbc.M608092200 (2006).
856 18 Kageyama-Yahara, N. & Riezman, H. Transmembrane topology of ceramide synthase in
857 yeast. *Biochem J* **398**, 585-593, doi:10.1042/bj20060697 (2006).
858 19 Venkataraman, K. & Futerman, A. H. Do longevity assurance genes containing Hox domains
859 regulate cell development via ceramide synthesis? *FEBS Lett* **528**, 3-4, doi:10.1016/s0014-
860 5793(02)03248-9 (2002).

20 Mesika, A., Ben-Dor, S., Laviad, E. L. & Futerman, A. H. A new functional motif in Hox domain-containing ceramide synthases: identification of a novel region flanking the Hox and TLC domains essential for activity. *J Biol Chem* **282**, 27366-27373, doi:10.1074/jbc.M703487200 (2007).

21 Sassa, T., Hirayama, T. & Kihara, A. Enzyme Activities of the Ceramide Synthases CERS2-6 Are Regulated by Phosphorylation in the C-terminal Region. *J Biol Chem* **291**, 7477-7487, doi:10.1074/jbc.M115.695858 (2016).

22 Tidhar, R. *et al.* Eleven residues determine the acyl chain specificity of ceramide synthases. *J Biol Chem* **293**, 9912-9921, doi:10.1074/jbc.RA118.001936 (2018).

23 Laviad, E. L., Kelly, S., Merrill, A. H., Jr. & Futerman, A. H. Modulation of ceramide synthase activity via dimerization. *J Biol Chem* **287**, 21025-21033, doi:10.1074/jbc.M112.363580 (2012).

24 Jensen, S. A. *et al.* Bcl2L13 is a ceramide synthase inhibitor in glioblastoma. *Proc Natl Acad Sci U S A* **111**, 5682-5687, doi:10.1073/pnas.1316700111 (2014).

25 Kim, J. L. *et al.* Fatty acid transport protein 2 interacts with ceramide synthase 2 to promote ceramide synthesis. *Journal of Biological Chemistry* **298**, 101735, doi:10.1016/j.jbc.2022.101735 (2022).

26 Cingolani, F., Futerman, A. H. & Casas, J. Ceramide synthases in biomedical research. *Chem Phys Lipids* **197**, 25-32, doi:10.1016/j.chemphyslip.2015.07.026 (2016).

27 Marasas, W. F. *et al.* Fumonisins disrupt sphingolipid metabolism, folate transport, and neural tube development in embryo culture and in vivo: a potential risk factor for human neural tube defects among populations consuming fumonisin-contaminated maize. *J Nutr* **134**, 711-716, doi:10.1093/jn/134.4.711 (2004).

28 Riley, R. T. & Merrill, A. H., Jr. Ceramide synthase inhibition by fumonisins: a perfect storm of perturbed sphingolipid metabolism, signaling, and disease. *J Lipid Res* **60**, 1183-1189, doi:10.1194/jlr.S093815 (2019).

29 Riley, R. T. *et al.* Fumonisins (addendum). 415–573 (World Health Organization, Geneva, Switzerland, 2018).

30 Merrill, A. H., Jr., van Echten, G., Wang, E. & Sandhoff, K. Fumonisin B1 inhibits sphingosine (sphinganine) N-acyltransferase and de novo sphingolipid biosynthesis in cultured neurons in situ. *J Biol Chem* **268**, 27299-27306 (1993).

31 Berdyshev, E. V. *et al.* FTY720 Inhibits Ceramide Synthases and Up-regulates Dihydrosphingosine 1-Phosphate Formation in Human Lung Endothelial Cells. *Journal of Biological Chemistry* **284**, 5467-5477, doi:10.1074/jbc.m805186200 (2009).

32 Lahiri, S. *et al.* Ceramide synthesis is modulated by the sphingosine analog FTY720 via a mixture of uncompetitive and noncompetitive inhibition in an Acyl-CoA chain length-dependent manner. *J Biol Chem* **284**, 16090-16098, doi:10.1074/jbc.M807438200 (2009).

33 Turner, N. *et al.* A selective inhibitor of ceramide synthase 1 reveals a novel role in fat metabolism. *Nature Communications* **9**, 3165, doi:10.1038/s41467-018-05613-7 (2018).

34 Nie, L. *et al.* The structural basis of fatty acid elongation by the ELOVL elongases. *Nature Structural & Molecular Biology* **28**, 512-520, doi:10.1038/s41594-021-00605-6 (2021).

35 Niu, Y. *et al.* Analysis of the mechanosensor channel functionality of TACAN. *eLife* **10**, e71188 , citation = eLife 72021;71110 e71188, doi:10.7554/eLife.71188 (2021).

36 Ke, M. *et al.* Cryo-EM structures of human TMEM120A and TMEM120B. *Cell Discov* **7**, 77, doi:10.1038/s41421-021-00319-5 (2021).

37 Holm, L., Laiho, A., Törönen, P. & Salgado, M. DALI shines a light on remote homologs: One hundred discoveries. *Protein Sci* **32**, e4519, doi:10.1002/pro.4519 (2023).

38 Ikeda, M. *et al.* Characterization of four mammalian 3-hydroxyacyl-CoA dehydratases involved in very long-chain fatty acid synthesis. *FEBS Letters* **582**, 2435-2440, doi:10.1016/j.febslet.2008.06.007 (2008).

39 Cleland, W. W. The kinetics of enzyme-catalyzed reactions with two or more substrates or products. I. Nomenclature and rate equations. *Biochim Biophys Acta* **67**, 104-137, doi:10.1016/0006-3002(63)91800-6 (1963).
40 Zollinger, M. *et al.* Absorption and disposition of the sphingosine 1-phosphate receptor modulator fingolimod (FTY720) in healthy volunteers: a case of xenobiotic biotransformation following endogenous metabolic pathways. *Drug Metab Dispos* **39**, 199-207, doi:10.1124/dmd.110.035907 (2011).
41 Wedekind, J. E., Frey, P. A. & Rayment, I. The structure of nucleotidylated histidine-166 of galactose-1-phosphate uridylyltransferase provides insight into phosphoryl group transfer. *Biochemistry* **35**, 11560-11569, doi:10.1021/bi9612677 (1996).
42 Zhou, X. *et al.* Kinetic Mechanism of Human Histidine Triad Nucleotide Binding Protein 1. *Biochemistry* **52**, 3588-3600, doi:10.1021/bi301616c (2013).
43 Trent, M. S., Worsham, L. M. S. & Ernst-Fonberg, M. L. HlyC, the Internal Protein Acyltransferase That Activates Hemolysin Toxin: Roles of Various Conserved Residues in Enzymatic Activity As Probed by Site-Directed Mutagenesis. *Biochemistry* **38**, 9541-9548, doi:10.1021/bi9905617 (1999).
44 Dodds, A. W., Ren, X. D., Willis, A. C. & Law, S. K. The reaction mechanism of the internal thioester in the human complement component C4. *Nature* **379**, 177-179, doi:10.1038/379177a0 (1996).
45 Gadjeva, M. *et al.* The covalent binding reaction of complement component C3. *J Immunol* **161**, 985-990 (1998).
46 Selvy, P. E., Lavieri, R. R., Lindsley, C. W. & Brown, H. A. Phospholipase D: enzymology, functionality, and chemical modulation. *Chem Rev* **111**, 6064-6119, doi:10.1021/cr200296t (2011).
47 Vanni, N. *et al.* Impairment of ceramide synthesis causes a novel progressive myoclonus epilepsy. *Ann Neurol* **76**, 206-212, doi:10.1002/ana.24170 (2014).
48 Harrer, H., Laviad, E. L., Humpf, H. U. & Futerman, A. H. Identification of N-acyl-fumonisin B1 as new cytotoxic metabolites of fumonisin mycotoxins. *Mol Nutr Food Res* **57**, 516-522, doi:10.1002/mnfr.201200465 (2013).
49 Harrer, H., Humpf, H. U. & Voss, K. A. In vivo formation of N-acyl-fumonisin B1. *Mycotoxin Res* **31**, 33-40, doi:10.1007/s12550-014-0211-5 (2015).
50 Zelnik, I. D. *et al.* Computational design and molecular dynamics simulations suggest the mode of substrate binding in ceramide synthases. *Nat Commun* **14**, 2330, doi:10.1038/s41467-023-38047-x (2023).
51 Youssefian, L. *et al.* Autosomal recessive congenital ichthyosis: CERS3 mutations identified by a next generation sequencing panel targeting ichthyosis genes. *Eur J Hum Genet* **25**, 1282-1285, doi:10.1038/ejhg.2017.137 (2017).
52 Eckl, K. M. *et al.* Impaired epidermal ceramide synthesis causes autosomal recessive congenital ichthyosis and reveals the importance of ceramide acyl chain length. *J Invest Dermatol* **133**, 2202-2211, doi:10.1038/jid.2013.153 (2013).
53 Radner, F. P. *et al.* Mutations in CERS3 cause autosomal recessive congenital ichthyosis in humans. *PLoS Genet* **9**, e1003536, doi:10.1371/journal.pgen.1003536 (2013).
54 Dougherty, D. A. The cation-π interaction. *Acc Chem Res* **46**, 885-893, doi:10.1021/ar300265y (2013).
55 Merrill, A. H., Jr., Wang, E., Gilchrist, D. G. & Riley, R. T. Fumonisins and other inhibitors of de novo sphingolipid biosynthesis. *Adv Lipid Res* **26**, 215-234 (1993).
56 Xie, T. *et al.* Structure and mechanism of a eukaryotic ceramide synthase complex. *Embo j*, e114889, doi:10.15252/embj.2023114889 (2023).
57 Tidhar, R., Sims, K., Rosenfeld-Gur, E., Shaw, W. & Futerman, A. H. A rapid ceramide synthase activity using NBD-sphinganine and solid phase extraction. *J Lipid Res* **56**, 193-199, doi:10.1194/jlr.D052001 (2015).

58 Geertsma, E. R., Nik Mahmood, N. A., Schuurman-Wolters, G. K. & Poolman, B. Membrane reconstitution of ABC transporters and assays of translocator function. *Nat Protoc* **3**, 256-266, doi:10.1038/nprot.2007.519 (2008).
59 Hutter, C. A. J. *et al.* The extracellular gate shapes the energy profile of an ABC exporter. *Nature Communications* **10**, 2260, doi:10.1038/s41467-019-09892-6 (2019).
60 Pardon, E. *et al.* A general protocol for the generation of Nanobodies for structural biology. *Nature Protocols* **9**, 674-693, doi:10.1038/nprot.2014.039 (2014).
61 Zheng, S. Q. *et al.* MotionCor2: anisotropic correction of beam-induced motion for improved cryo-electron microscopy. *Nat Methods* **14**, 331-332, doi:10.1038/nmeth.4193 (2017).
62 Punjani, A., Rubinstein, J. L., Fleet, D. J. & Brubaker, M. A. cryoSPARC: algorithms for rapid unsupervised cryo-EM structure determination. *Nat Methods* **14**, 290-296, doi:10.1038/nmeth.4169 (2017).
63 Punjani, A., Zhang, H. & Fleet, D. J. Non-uniform refinement: adaptive regularization improves single-particle cryo-EM reconstruction. *Nat Methods* **17**, 1214-1221, doi:10.1038/s41592-020-00990-8 (2020).
64 Asarnow, D., Palovcak, E. & Cheng, Y. *UCSF pyem v0.5*, <https://doi.org/10.5281/zenodo.3576630}> (2019).
65 Zivanov, J. *et al.* New tools for automated high-resolution cryo-EM structure determination in RELION-3. *Elife* **7**, doi:10.7554/eLife.42166 (2018).
66 Jumper, J. *et al.* Highly accurate protein structure prediction with AlphaFold. *Nature* **596**, 583-589, doi:10.1038/s41586-021-03819-2 (2021).
67 Kelley, L. A., Mezulis, S., Yates, C. M., Wass, M. N. & Sternberg, M. J. The Phyre2 web portal for protein modeling, prediction and analysis. *Nat Protoc* **10**, 845-858, doi:10.1038/nprot.2015.053 (2015).
68 Emsley, P., Lohkamp, B., Scott, W. G. & Cowtan, K. Features and development of Coot. *Acta crystallographica. Section D, Biological crystallography* **66**, 486-501, doi:10.1107/S0907444910007493 (2010).
69 Afonine, P. V. *et al.* Real-space refinement in PHENIX for cryo-EM and crystallography. *Acta Crystallogr D Struct Biol* **74**, 531-544, doi:10.1107/s2059798318006551 (2018).
70 Long, F. *et al.* AceDRG: a stereochemical description generator for ligands. *Acta Crystallogr D Struct Biol* **73**, 112-122, doi:10.1107/s2059798317000067 (2017).
71 Yamashita, K., Palmer, C. M., Burnley, T. & Murshudov, G. N. Cryo-EM single-particle structure refinement and map calculation using Servalcat. *Acta Crystallogr D Struct Biol* **77**, 1282-1291, doi:10.1107/s2059798321009475 (2021).
72 Burnley, T., Palmer, C. M. & Winn, M. Recent developments in the CCP-EM software suite. *Acta Crystallogr D Struct Biol* **73**, 469-477, doi:10.1107/s2059798317007859 (2017).
73 Tautermann, C. S. *et al.* Allosteric Activation of Striatal-Enriched Protein Tyrosine Phosphatase (STEP, PTPN5) by a Fragment-like Molecule. *J Med Chem* **62**, 306-316, doi:10.1021/acs.jmedchem.8b00857 (2019).
74 Lu, C. *et al.* OPLS4: Improving Force Field Accuracy on Challenging Regimes of Chemical Space. *J Chem Theory Comput* **17**, 4291-4300, doi:10.1021/acs.jctc.1c00302 (2021).
75 Schrodinger, LLC. *The PyMOL Molecular Graphics System, Version 2.1* (2015).
76 Pettersen, E. F. *et al.* UCSF ChimeraX: Structure visualization for researchers, educators, and developers. *Protein Sci* **30**, 70-82, doi:10.1002/pro.3943 (2021).